J. Fluid Mech. (1986), *vol.* 166, *pp.* 57–92
Printed in Great Britain

Shock waves and phase changes in a large-heat-capacity fluid emerging from a tube

By PHILIP A. THOMPSON,
Rensselaer Polytechnic Institute, Troy, NY 12181

GARRY C. CAROFANO
Benet Weapons Laboratory, Watervliet, NY 12189

AND YOON-GON KIM
Rensselaer Polytechnic Institute, Troy, NY 12181

(Received 21 May 1985 and in revised form 21 October 1985)

The emergence of a shockwave from the open end of a shock tube is studied, with special emphasis on test fluids of high molar heat capacity, i.e. retrograde fluids. A variety of wavelike vapour–liquid phase changes are observed in such fluids, including the liquefaction shock, mixture-evaporation shock, condensation waves associated with shock splitting and liquid-evaporation waves (these phenomena have analogues in the polymorphic phase changes of solids; only the first two are treated in this paper). The open end of the shock-tube test section discharges into an observation chamber where photographs of the emerging flow are taken. Calculations were performed with the Benedict–Webb–Rubin, van der Waals and other equations of state. Numerical (finite-difference) predictions of the flow were made for single-phase and two-phase flows: solutions were tested against the experimental shock diffraction and vortex data of Skews. The phase-change properties of the test fluid can be quantified by the 'retrogradicity' $r(T)$, measuring the difference in slope between the P, T isentrope and the vapour-pressure curve, and the 'kink' $k(T)$, measuring the difference between the single-phase and mixture sound speeds. Mixture-evaporation (i.e. rarefaction) shocks appear to have a sonic–sonic or double Chapman–Jouguet structure and show agreement with amplitude predictions based on $k(T)$. Liquefaction shocks are found to show a reproducible transition from regular, smooth shock fronts to irregular, chaotic shock fronts with increasing shock Mach number. This transition can be correlated with published stability limits.

1. Introduction

A variety of phase changes proceed spontaneously and often quite rapidly from a metastable state, without the need for significant heat transfer. Examples include the condensation of water vapour in a supersonic nozzle, achieved by the rapid isentropic expansion of the flowing vapour to a (metastable) state of supersaturation; the commercial production of 'dry ice' by a similar expansion of CO_2 gas; condensation in a cloud chamber; bubble formation in a hydrogen bubble chamber; cavitation around the screw propeller of a ship. In all of these examples, the required metastable state is produced by a rapid reduction in pressure, that is an expansion flow. The metastable state can be produced by other means, as in the case of a bubble column for vapour-explosion research, in which tiny liquid drops are slowly heated to the spinodal limit of thermodynamic stability, where explosive evaporation occurs.

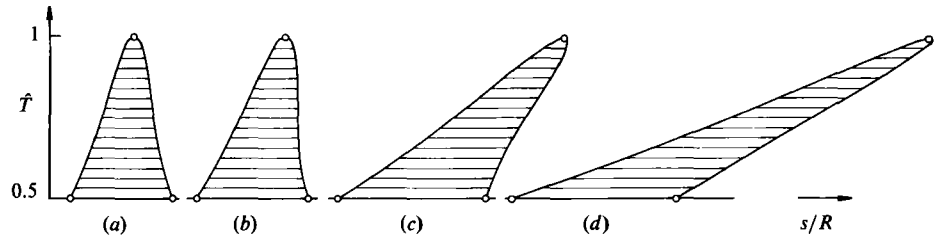

FIGURE 1. Temperature–entropy diagrams of substances with increasing characteristic heat capacities $\tilde{c}_v$. The reduced temperature $\hat{T}$ ranges from 0.5 to the critical-point value 1.0. Only the liquid and vapour-saturation boundaries are shown. (*a*) Ethene C_2H_4, $\tilde{c}_v = 4.03$; (*b*) Propane C_3H_8, $\tilde{c}_v = 9.64$; (*c*) *n*-Octane C_8H_{18}, $\tilde{c}_v = 36.82$; (*d*) Pf-methyldecaline $C_{11}F_{20}$, $\tilde{c}_v = 73.4$.

The work discussed here deals chiefly with shock-induced vapour–liquid phase changes in fluids with large molar heat capacities, i.e. fluids with many molecular degrees of freedom, octane for example. The vapours of such fluids tend to condense on adiabatic *compression* (retrograde behaviour), as distinct from the vapours of fluids of lower heat capacity, such as water, which tend to condense on adiabatic *expansion* (regular behaviour). For liquid–vapour systems showing retrograde behaviour, many of the accepted rules of gasdynamics are inverted and new phenomena appear, e.g. the liquefaction shock wave described by Dettleff *et al.* (1979).

The distinction between retrograde behaviour (for fluids such as octane) and regular behaviour (for fluids such as water) is essential to the substance of this paper and will be further discussed in §2. Here the distinction is illustrated by the temperature–entropy diagrams shown in figure 1. The substances illustrated show the typical tendency for the saturated-vapour boundary σ to lean over to the right, such that $(\mathrm{d}s/\mathrm{d}T)_\sigma$ takes on positive values (retrograde behaviour) with increasing heat capacity c_v. It is convenient to assign each substance a characteristic heat capacity

$$\tilde{c}_v \equiv \frac{c_v^0(T_c)}{R}, \tag{1}$$

i.e. the ideal-gas heat capacity at the thermodynamic critical temperature T_c, normalized by the gas constant R (in general, the non-dimensional heat capacity c_v/R will be denoted $\hat{c}_v$). Compression of the vapour will lead to condensation for sufficiently large values of $\tilde{c}_v$, because the work of compression produces a correspondingly small increase in temperature: in this case, the behaviour is 'retrograde', as typified by octane in figure 1. For smaller values of $\tilde{c}_v$, compression of the vapour will lead to such a large temperature rise that no condensation is possible: the behaviour is 'regular' as typified by ethene and other common substances such as air and steam.

Retrograde phase changes, in the general sense of an adiabatic transition to a denser phase under increasing pressure, are often found in solids in association with shock waves (Zel'dovich & Raizer 1967; Davidson & Graham 1979). The synthesis of industrial-grade diamond from graphite is one specific example (McQueen & Marsh 1968; Morris 1980). The 'ice-skating' transition from ice to water when the ice is subjected to increasing pressure is a solid–liquid example.

A brief inspection of a temperature–entropy diagram such as figure 1 (*d*) suggests the possibility of various adiabatic phase changes in retrograde liquid–vapour systems. Several forms of wave-induced phase changes have recently been studied and observed. The following list refers especially to liquid–vapour systems; it also applies by extension to analogous solid–solid, solid–liquid and other systems.

Liquefaction shock. A transition from vapour to liquid takes place across a compression shock wave (Thompson & Sullivan 1975; Dettleff 1978; Dettleff *et al.* 1979, 1982). If the phase transition is complete across the wave, it is called a *complete* liquefaction shock; otherwise, it is called a *partial* liquefaction shock.

Shock splitting. A single, partial liquefaction shock splits into two discrete waves, which then diverge from each other (Thompson & Kim 1983; Speckmann 1984; Thompson, Kim & Meier 1984). The first wave of the split-shock system is called the *forerunner shock*, the following wave the *condensation discontinuity* or condensation shock. In the linear, equilibrium description of shock splitting, the forerunner shock and the condensation discontinuity propagate at the saturated-vapour sound speed and the mixture sound speed respectively.

Rarefaction shock. A rarefaction wave steepens to form a rarefaction-shock discontinuity. In the single-phase case, this will occur in the neighbourhood of regions of negative nonlinearity, as discussed by Thompson & Lambrakis (1973) and by Cramer & Kluwick (1984). In the two-phase case, the rarefaction shock will bridge two points on each side of the saturated-vapour boundary, the upstream state lying in the mixture region and the downstream state lying in the superheated-vapour region.

Complete evaporation shock. A liquid is evaporated completely across a rarefaction shock. Solutions of this type exist for van der Waals fluids (Slemrod 1983, 1984). Solutions for non-equilibrium upstream states near the liquid spinodal show a double Chapman–Jouguet structure. No experimental results corresponding to these models are known to the authors.

Liquid-evaporation waves. Sudden reduction of the pressure on a liquid produces a superheated metastable state, followed by evaporation. In the experiments of Chaves (1980, 1984), the initial reduction of pressure takes place across a sharp forerunner expansion wave propagating into the liquid; this is followed by an evaporation discontinuity which propagates more slowly and is analogous to a Chapman–Jouguet deflagration. The two-wave system is thus another example of wave splitting.

The possible states upstream and downstream of these discontinuities are listed in table 1. Several of the phenomena described above are interrelated: both shock splitting and rarefaction shocks follow the (inverted) rule that compression waves spread out in regions of negative nonlinearity (this terminology is formally defined in §2). The forerunner wave and the liquid-evaporation wave found by Chaves have distinct similarities with the waves treated here. Both the condensation discontinuity and the evaporation wave show detonation-type adiabats, corresponding to non-equilibrium upstream states. Although the condensation wave releases latent heat into the vapour and the evaporation wave takes up latent heat from the liquid, these adiabats are 'endothermic' and 'exothermic' respectively, in the conventional terminology (Hayes 1958).

Chapman–Jouguet solutions are found experimentally in evaporation waves (Chaves 1984) and appear to be present in rarefaction shocks. The asymptotic Chapman–Jouguet solutions found for abrupt condensation in supersaturated steam by Wegener & Mack (1958) are, of course, not found here, by virtue of the 'endothermic' adiabat form.

Additional phenomena not described here are likely to be especially interesting in retrograde cases – vapour explosions, for example, would be expected to show greater strength, because the energy stored in the liquid at a given superheat increases with the liquid heat capacity.

Discontinuity	Upstream state	Downstream state
Liquefaction shock	Vapour	Equilibrium mixture or liquid
Forerunner shock	Vapour	Supersaturated vapour
Condensation discontinuity	Supersaturated vapour	Equilibrium mixture
Rarefaction shock	Vapour or equilibrium mixture	Vapour
Forerunner wave	Saturated liquid	Superheated liquid
Liquid-evaporation wave	Superheated liquid	Equilibrium mixture

TABLE 1. Summary of states at a discontinuity

It is remarkable that many of the rules of ordinary gasdynamics are inverted simply by increasing the heat capacity of the fluid. This may help to explain why several of the phenomena described above have been judged impossible. Bethe (1942) ruled out shock splitting and rarefaction shocks in fluids, Landau & Lifshitz (1959) did the same for liquefaction shocks; certain textbooks 'demonstrate' the impossibility of rarefaction shocks, usually based on a second-law argument.

Although retrograde phase changes are usual in many and diverse two-phase systems, they represent a marked departure from past experience in liquid–vapour systems. Whether the novelty of these phase changes will find proportionate technical or scientific relevance remains to be seen.

In small-scale Rankine-cycle heat engines (in the range of 10–50 kW, say) there is a case for multiatomic, retrograde working fluids. The flow behaviour in the turbines and compressors of such engines can be predicted on the basis of further experimental and analytical studies. In hydrocarbon-fuel combustion, interesting possibilities exist for the generation of vapour-phase fuel (and consequent efficient combustion) by fast adiabatic evaporation, related to the laboratory experiments of Chaves (1980, 1984). This applies to fuel injection of internal combustion engines in particular; retrograde phase changes may also be pertinent to the transient events within a piston engine. In separation processes, the behaviour of simple devices such as centrifugal-effect separation nozzles (Ehrfeld 1983) may be favourably influenced by partial liquefaction on the outer perimeter. Finally, rapid heating as achieved in a liquefaction shock (accompanied by a large increase in density) could be used, for example, to 'switch on' organic chemical reactions: in a transient process like the one at the closed end of a shock tube, the reaction would then be switched off or quenched after a few milliseconds.

Applicability to scientific studies could also be mentioned. It is possible to produce a short-duration critical state behind a liquefaction shock, for example at the closed end of a shock tube, and by this means measure the critical temperature and pressure of thermally unstable organic fluids. Two-phase sound-speed measurements are discussed in this paper in a later section. Critical-supersaturation experiments are especially convenient and could provide nucleation specialists with a new field for validating theoretical models. Convection experiments in gravitational or centrifugal-force fields should prove especially interesting for retrograde fluid systems, simply because condensation occurs with increasing (rather than decreasing) pressure: in a retrograde atmosphere, cumulus clouds would sink toward the surface of a planet before producing precipitation, rather than rising. Finally, the many flow instabilities found in dynamic retrograde phase changes offer interesting challenges in fundamental fluid dynamics: the tiny vortex rings observed near the liquefaction shock front (Dettleff *et al.* 1979, 1982) appear to provide a rare example of a molecular event (nucleation) manifested in a macroscopic instability.

2. Regular and retrograde behaviour

With increasing molecular complexity, the familiar bell-shaped saturation curve of a temperature–entropy diagram slopes over to the right, as shown in figure 1. This behaviour is described by the following identity for the slope of the liquid and vapour-saturation boundaries:

$$T\left(\frac{\mathrm{d}s}{\mathrm{d}T}\right)_\sigma = c_v + T\left(\frac{\partial P}{\partial T}\right)_v \left(\frac{\mathrm{d}v}{\mathrm{d}T}\right)_\sigma. \tag{2}$$

Partial derivatives and heat capacities correspond to single-phase values in the region immediately adjacent to the saturation boundary σ (i.e. liquid or vapour, the latter being emphasized in the following) and the subscript σ refers to saturation properties. On the liquid side, both of the right-hand terms are positive right up to the critical point and the slope given by (2) is positive. On the vapour side, the first right-hand term c_v is always positive and the second term is always negative. For sufficiently large values of the vapour c_v, the slope given by (2) can then become positive, corresponding to retrograde behaviour. Near the critical point on the vapour side, however, the slope $(\mathrm{d}s/\mathrm{d}T)_\sigma$ will always be negative, because the value of $(\mathrm{d}v/\mathrm{d}t)_\sigma$ approaches $-\infty$ much more rapidly than c_v approaches $+\infty$, as described by the respective critical exponents (the above statement also holds for a classical van der Waals description, in which c_v remains finite). These features are illustrated in figure 2 for the case of benzene. Between points A and B on the saturated-vapour boundary, the phase-change behaviour is retrograde.

From corresponding-states calculations (Lambrakis 1972), it is found that the saturated-vapour boundary just reaches the vertical ($\mathrm{d}s/\mathrm{d}T$ has a value of zero) for $\tilde{c}_v = 11.2$, a value which happens to correspond to sulfur hexafluoride SF_6 and falls between propane and butane in the alkane-series hydrocarbons. Benzene, with a characteristic heat capacity $\tilde{c}_v = 17.1$, thus shows a limited degree of regtrograde behaviour. In order to quantify the 'retrogradicity', it is convenient to introduce the non-dimensional parameter $r(T)$,

$$r(T) \equiv \left(\frac{\partial T}{\partial v}\right)_p \left(\frac{\mathrm{d}s}{\mathrm{d}P}\right)_\sigma, \tag{3}$$

where the partial derivative refers to the value in the single-phase region (vapour in the present case) adjacent to the saturation boundary σ and the total derivative refers to the variation along the saturation boundary, as in (2). Because the slope $(\mathrm{d}P/\mathrm{d}T)_\sigma$ of the vapour-pressure curve is positive, $r(T)$ will necessarily have the same sign as $(\mathrm{d}s/\mathrm{d}T)_\sigma$, provided that the thermal-expansion derivative $(\partial v/\partial T)_p > 0$. Thus, retrograde behaviour is normally associated with $r > 0$ and regular behaviour with $r < 0$ on the vapour boundary. The behaviour of $r(T)$ along the saturated-vapour boundary of figure 2, with $r > 0$ between A and B, $r = 0$ at A and B, and $r < 0$ above A and below B, is characteristic of all fluids showing retrograde behaviour. The dependence of such behaviour on the single-phase heat capacity can be shown by writing (3) in the form

$$r(T) = \frac{c_p}{T}\left(\frac{\partial T}{\partial v}\right)_p \left(\frac{\mathrm{d}T}{\mathrm{d}P}\right)_\sigma - 1, \tag{4}$$

in which the coefficient c_p plays the dominant role in fixing the magnitude of the product on the right-hand side. Using the Clapeyron equation, (4) can be rewritten as

$$r(T) = c_p \left(\frac{\partial T}{\partial v}\right)_p \frac{v_{\mathrm{lv}}}{L} - 1, \tag{5}$$

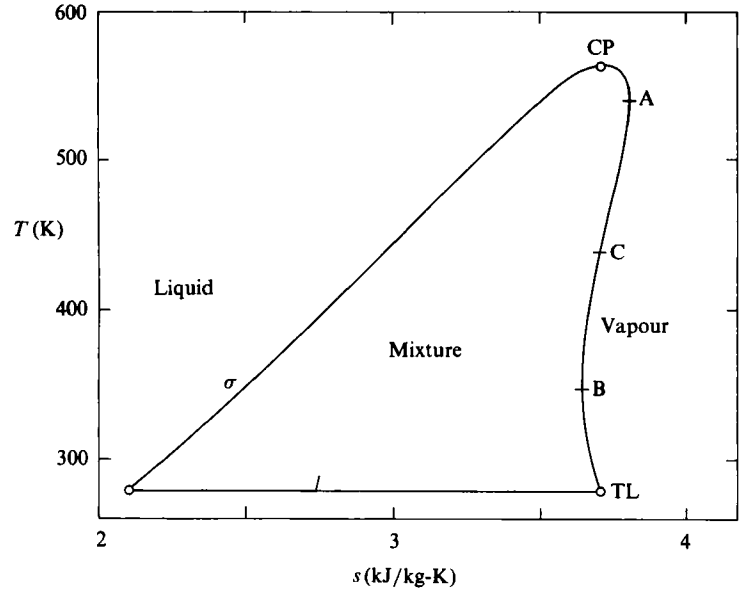

FIGURE 2. Temperature–entropy diagram for benzene. Physical properties at the critical point: $T_c = 562.16$ K, $P_c = 48.98$ bar, $\tilde{c}_v = 17.09$. The triple temperature is $T_{tl} = 278.68$ K. The point C on the saturated-vapour boundary has the same entropy as the critical point CP. Maximum and minimum entropy on the saturated-vapour boundary are at A and B respectively (Anon 1973).

where $v_{lv}(T)$ is the volume change on evaporation and $L(T)$ is the latent heat (enthalpy of vaporization). In the low-pressure approximation, corresponding to an ideal-gas vapour and the Clausius–Clapeyron equation, this reduces to

$$r(T) = \frac{c_p^0 T}{L} - 1. \tag{6}$$

The parameter in this form often occurs in heat-transfer problems with phase change, see for example Knuth (1959) and Kosky (1968). Equation (6) illustrates nicely a basis for retrograde behaviour, that the energy stored in the molecular degrees of freedom be large compared to the latent heat. For nonlinear molecules containing n atoms, the ideal-gas heat capacity c_p^0 approaches a maximum value $(3n\text{-}2)R$ with increasing temperature. The latent heat L is independent of molecular complexity in the first approximation and depends on reduced temperature $\hat{T}$ according to (Reid, Prausnitz & Sherwood 1977) $L = RT_c f(\hat{T})$, where R is the gas constant, T_c is the critical temperature; $f(T)$ decreases monotonically with temperature, vanishing at the critical point where $\hat{T} = 1$. According to (6), r thus tends to increase with temperature, because both $c_p^0(T)$ and T/L are increasing, and to increase with molecular complexity. Thus, substances with sufficiently large values of $\tilde{c}_v$ will always show retrograde behaviour over some part of the temperature range of liquid–vapour coexistence. All substances will show regular behaviour at very low reduced temperatures and again at high reduced temperatures, where the $(\mathrm{d}v/\mathrm{d}T)_\sigma$ term in (2) will dominate.

Regular and retrograde behaviour can be conveniently represented in the pressure–temperature plane, as shown in figure 3. The retrogradicity $r(T)$ defined in (3) can be expressed in the appropriate form

$$r(T) = \frac{(\partial P/\partial T)_s - (\mathrm{d}P/\mathrm{d}T)_\sigma}{(\mathrm{d}P/\mathrm{d}T)_\sigma}, \tag{7}$$

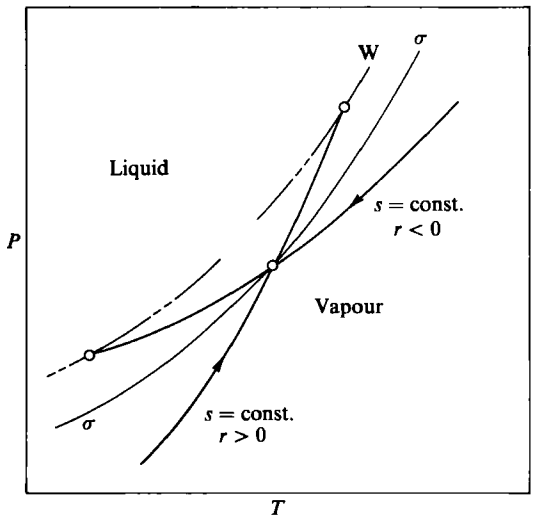

FIGURE 3. Pressure–temperature diagram, combined for regular ($r < 0$) and retrograde ($r > 0$) fluids. The vapour–pressure curve is labelled σ and the Wilson line W. Vapour states of supersaturation are approximately bounded by σ and W.

which describes the difference in slopes between isentropes and the vapour-pressure curve σ. For $r > 0$, isentropes are steeper than the vapour-pressure curve and condensation occurs on compression; for $r < 0$, isentropes are less steep than the vapour-pressure curve and condensation occurs on expansion, as in supersonic-nozzle experiments (for example Wegener & Wu 1977). In figure 3, the isentropes are extended across the saturation boundary, corresponding to supersaturated vapour states, to the curve of spontaneous homogeneous nucleation or 'Wilson line'. These non-equilibrium states are found in supersonic-nozzle and other expansion experiments and play an important role in shock splitting.

2.1. *Condensation of supersaturated vapour*

The delayed condensation of metastable (supersaturated) vapour originates at a point near the Wilson line, where the nucleation rate becomes so large that condensation is manifested, for example, by light scattering or the appearance of visible condensate, as in the case of the liquefaction shock. To illustrate the role of retrograde behaviour in spontaneous condensation, it is useful to ask the following question: Given an initial supersaturated-vapour state P_1, v_1, what equilibrium state P_2, v_2 will then be reached by spontaneous condensation? This question is here simplified as follows: to find the isobaric state P_1, v_2 reached across a condensation discontinuity with negligible momentum effects, i.e. using the low-velocity or flame-front approximation. We thus seek to find the volume change $v_2 - v_1$. A convenient measure of the initial supersaturation in this case is $v_\sigma - v_1$, where v_σ is the saturated-vapour volume at pressure P_1 (see figure 4). From Taylor expansions about state σ, using the metastable-vapour coefficients for state (1) and equilibrium-mixture coefficients for state (2) and the Rankine–Hugoniot condition $h_2 - h_1 = 0$,

$$v_2 - v_1 = -r(v_\sigma - v_1) + O(v_\sigma - v_1)^2, \tag{8}$$

where $r = r[T_\sigma(P_1)]$ is the 'retrogradicity' previously described. The equilibrium, downstream state (II) will thus be more dense than the metastable, upstream state

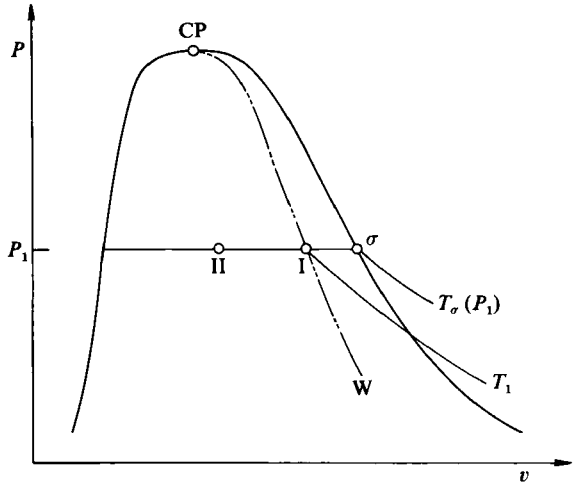

FIGURE 4. Pressure–volume diagram illustrating constant-pressure condensation from a supersaturated-vapour state (I) on the Wilson line W to a mixture equilibrium state (II).

(I) if $r > 0$ (retrograde) and less dense if $r < 0$ (regular). An important example of spontaneous condensation of a supersaturated vapour is cloud formation in a rising mass of warm, moist air ($r < 0$). The upward convection is driven by buoyancy, that is the density of the rising mass is less than that of the surrounding atmosphere. Upon spontaneous condensation, the density of the rising mass is further decreased and the upward convection is thereby enhanced (see (8)), along with the adiabatic cooling which produces the condensation. The process thus tends to be self-sustaining as long as moisture is available: it can be observed in the tops of growing cumulus clouds. In a retrograde atmosphere, on the other hand, clouds would grow on downward convection, enhanced by density increase on condensation.

The change in volume predicted by the first-order result (8) may be considered in terms of the competing effects of latent-heat release (promoting volume expansion) and the removal of vapour by condensation (promoting volume contraction). The overall volume change in (8) can be written as a difference,

$$v_2 - v_1 = \Delta_{\mathrm{lh}} - \Delta_{\mathrm{mr}}, \tag{9}$$

where $\Delta_{\mathrm{lh}} > 0$ is the volume expansion associated with latent-heat release and $\Delta_{\mathrm{mr}} > 0$ is the volume contraction associated with mass removal. The behaviour will be 'regular' or 'retrograde', depending on whether Δ_{lh} or Δ_{mr} dominates, respectively. For condensation of a mass fraction α, the magnitudes are $\Delta_{\mathrm{lh}} \approx (\partial v/\partial T)_p \Delta T \approx (\partial v/\partial T)_p \alpha L/c_p$ and $\Delta_{\mathrm{mr}} \approx \alpha v_{1\mathrm{v}}$. With these magnitudes and $\alpha = (v_\sigma - v_2)/v_{1\mathrm{v}}$. (5, 8) yield for the normalized volume change

$$\frac{\Delta_{\mathrm{mr}} - \Delta_{\mathrm{lh}}}{v_\sigma - v_1} \approx r, \tag{10}$$

a result which can be confirmed by combining (8) and (9) directly. Thus, in retrograde condensation ($r > 0$) the mass removal dominates; in regular condensation ($r < 0$) the latent-heat release dominates.

The temperature jump $T_2 - T_1$ for the spontaneous, constant-pressure condensation can be found by a procedure similar to that used to find (8). The result is

$$T_2 - T_1 = \left(\frac{\partial T}{\partial v}\right)_p (v_\sigma - v_1) + O(v_\sigma - v_1)^2. \tag{11}$$

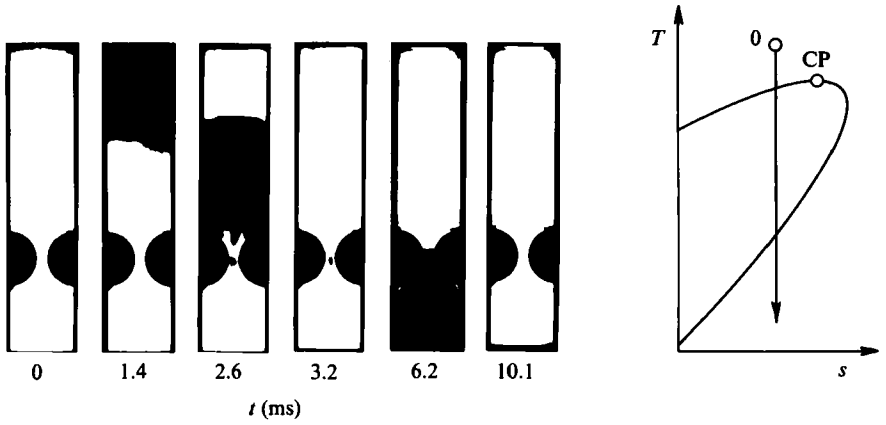

FIGURE 5. Expansion flow of supercritical vapour (n-C_6F_{14}) showing phase discontinuities. The temperature–entropy diagram shows the nearly isentropic expansion path. The arrow in the first photographic frame ($t = 0$) indicates the flow direction. Initial pressure $P_0 = 21$ bar. After Puettendoerfer (1982).

For ideal-gas vapour, the first-order result reduces to

$$\frac{T_2}{T_1} = \frac{v_\sigma}{v_1}. \tag{12}$$

The entropy jump $s_2 - s_1$ is given by

$$s_2 - s_1 = \frac{1}{2c_p}\left(\frac{\partial P}{\partial T}\right)_s^2 (v_\sigma - v_1)^2 + O(v_\sigma - v_1)^3. \tag{13}$$

Equations (8), (11), (12) and (13) represent special solutions for the gasdynamic condensation adiabat.

2.2. *A physical illustration of regular and retrograde condensation*

A simple, quasi-steady nozzle-flow experiment performed by Puettendoerfer (1982) is shown in figure 5. The expansion tube shown in the figure has a rectangular cross-section 15×20.8 mm wide and 110 mm long. It is closed at the top by a thin metal diaphragm which separates the tube from a large vacuum chamber above. It is closed at the bottom by a rigid wall and the two-dimensional nozzle is formed by semicircular metal inserts. The sidewalls are made of glass, so that two-phase regions appear as dark (opaque) regions in transmitted light. The test fluid is fluorinated n-Hexane, with properties similar to octane, maintained at a supercritical initial state (0) indicated in figure 5, such that an isentropic expansion from the high-pressure-vapour region passes into the mixture region and thence into the low-pressure-vapour region.

The flow, initiated by rupturing the diaphragm at time zero, is upward into the vacuum vessel and may be considered to originate from the small 'reservoir' in the lower part of the tube. The dynamic phase discontinuities, visible in the photographs as boundaries of the (opaque) mixture regions are approximately identical with the crossing points of the isentrope and the saturation boundary in figure 5. At time 2.6 ms, for example, the visible boundary between low-pressure vapour and mixture at the top of the photo corresponds to an evaporation (retrograde expansion) discontinuity, while the irregular lower boundary corresponds to a regular condensation.

2.3. *Discontinuity in the equilibrium sound speed at the saturation boundary*

In the liquid–vapour region adjacent to a saturation boundary, the isentropic compressibility of the mixture is increased over that of the single-phase fluid, that is the mixture is 'softer'. This can be understood in the case of a retrograde vapour, for example, where isentropic compression leads to condensation: a given pressure increase will produce a volume decrease of the vapour, augmented by the condensation of some fraction of the vapour.

The sound speed c, given by $c^2 = -v^2(\partial P/\partial v)_s$, is thus discontinuous at the saturation boundary. A measure of the jump magnitude is provided by the 'kink' k,

$$k(T) \equiv \frac{(\partial P/\partial v)_s - (\partial P/\partial v)_{sm}}{(\partial P/\partial v)_{sm}} = -\frac{T}{c_v}\left(\frac{\partial P}{\partial v}\right)_T \left(\frac{\mathrm{d}s}{\mathrm{d}P}\right)_\sigma^2 \geqslant 0, \tag{14}$$

where the subscript m refers to the equilibrium derivative on the mixture side of the saturation boundary σ and the other derivative corresponds to the single-phase value: thus, making use of the continuity of v at σ, k gives the difference between sound speeds at the saturation boundary in the form

$$k(T) = \frac{c^2 - c_{\mathrm{m}}^2}{c_{\mathrm{m}}^2} \geqslant 0, \tag{15}$$

where c is equilibrium sound speed. In figure 6(a), k is a measure of the difference in slopes of the equilibrium isentropes at point g on the saturated-vapour boundary. The equilibrium sound speed of the mixture is thus always smaller than or equal to that in the adjacent single-phase region. (The special case of equal sound speeds, corresponding to $k = 0$, occurs at points such as A and B in figure 2, where the isentrope is tangential to the saturation boundary.)

The 'kink' k and 'retrogradicity' r are related by

$$\frac{k}{r^2} = \frac{T}{c_v}\left(\frac{\partial P}{\partial T}\right)_v \left(\frac{\partial v}{\partial T}\right)_p = \gamma - 1 \geqslant 0, \tag{16}$$

where γ is the ratio of specific heats in the single phase. For $r > 0$, the equilibrium isentrope bends downward at the phase boundary, as shown in figure 6(a). This situation is associated with equilibrium-state shock splitting (Bethe 1942; Zel'dovich & Raizer 1967). For small-amplitude waves, it can be understood as a splitting into two compression discontinuities, a forerunner shock and a condensation shock, which propagate with velocities c and c_{m} respectively. Values of the parameters $r(T)$ and $k(T)$ are listed in table 2 and plotted in figure 7.

For sufficiently large $\tilde{c}_v$, the kink at the saturation boundary will be mimicked at higher pressures in the single-phase vapour region, as shown in figure 6(b), this behaviour being analogous to that of isotherms. The curvature of the isentrope is represented by the non-dimensional parameter Γ,

$$\Gamma \equiv \frac{-v^2(\partial^2 P/\partial v^2)_s}{2(\partial P/\partial v)_s}, \tag{17}$$

sometimes referred to as the fundamental gasdynamic derivative or nonlinearity parameter. For a perfect gas, $\Gamma = \frac{1}{2}(\gamma+1)$. For the special case in figure 6(b), $\Gamma < 0$ over a limited region G, analogous to $\Gamma = -\infty$ at the kink g on the saturated-vapour boundary. The condition $\Gamma < 0$ is necessary and sufficient for the existence of rarefaction shock waves (Bethe 1942; Zel'dovich 1946; Thompson & Lambrakis

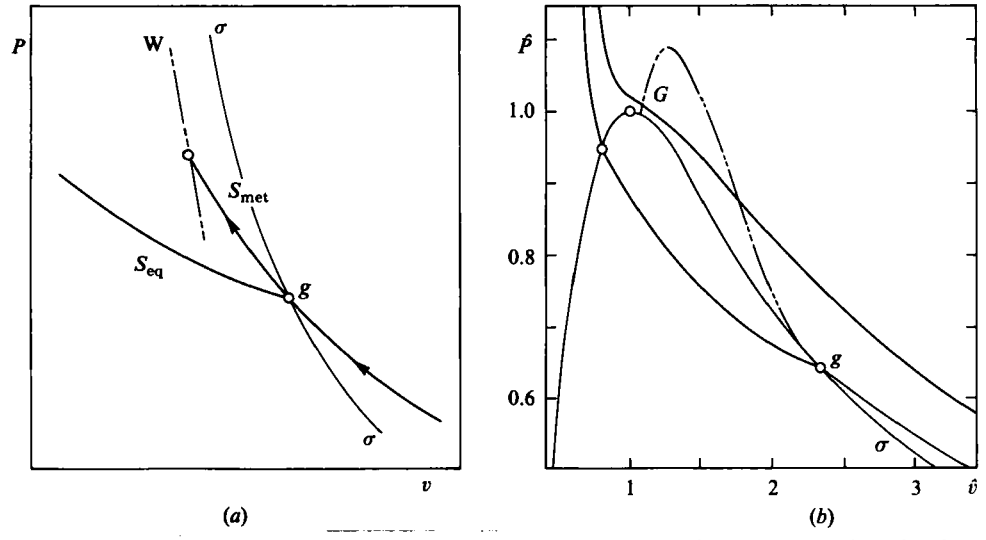

FIGURE 6. (*a*) Equilibrium and metastable isentropes at the saturated-vapour boundary for the case of retrograde behaviour ($r > 0$). W = Wilson line (supersaturation limit), σ = saturation boundary; (*b*) Analogy of a retrograde kink ($r > 0$) at g to $\Gamma < 0$ behaviour (in region G) at higher pressure in the single-phase vapour region. The isentropes shown are not to scale.

1973). A familiar material for which $\Gamma < 0$ is the ordinary stretched rubber band, where v in (17) is replaced by length l and P by the negative of tension. Indeed, rarefaction shocks are observed in this case (Kolsky 1969) and in other common materials, such as quartz (Barker & Hollenbach 1970).

In the experiments reported in this paper, rarefaction shocks are associated with the kink at point g in figure 6(*b*): the upstream states lie in the mixture region and the downstream states in the (dry) vapour region, so that the shock front is coincident with a phase discontinuity. The flow thus experiences sudden evaporation.

Although it is difficult to calculate reliable values of the fundamental derivative Γ for real substances (Thompson & Lambrakis 1973), an indication of the relation between retrograde behaviour ($r > 0$) and negative-Γ behaviour is provided by the minimum values of $\tilde{c}_v$ required to produce $r > 0$ and $\Gamma < 0$ (in the vapour region) for the van der Waals equation: these values for $\tilde{c}_v$ are 4.96 and 16.67 respectively. (It should be noted that this equation yields minimum values which are unrealistically small.)

Both Max Planck (1903) and van der Waals (1908) were aware of retrograde behaviour and its dependence on a large heat capacity, that is on many internal (vibrational) degrees of freedom. Bethe, however, dismissed the possibility of such fluids in his celebrated report (Bethe 1942) and thus reached formally incorrect conclusions about phenomena such as shock splitting. Of the known fluids, however, the great majority are retrograde: this can be verified by counting the substances listed in *Chemical Abstracts* with more than four carbon atoms, for example. Of the known solid and solid–liquid systems, the majority are retrograde, including the minerals of which the Earth is made.

3. Experimental arrangement

The shock tube has proven convenient for the production and study of liquefaction shocks. In the experiments of Dettleff *et al.* (1979), performed at the Max-Planck-Institut fuer Stroemungsforschung in Goettingen, partial and complete liquefaction

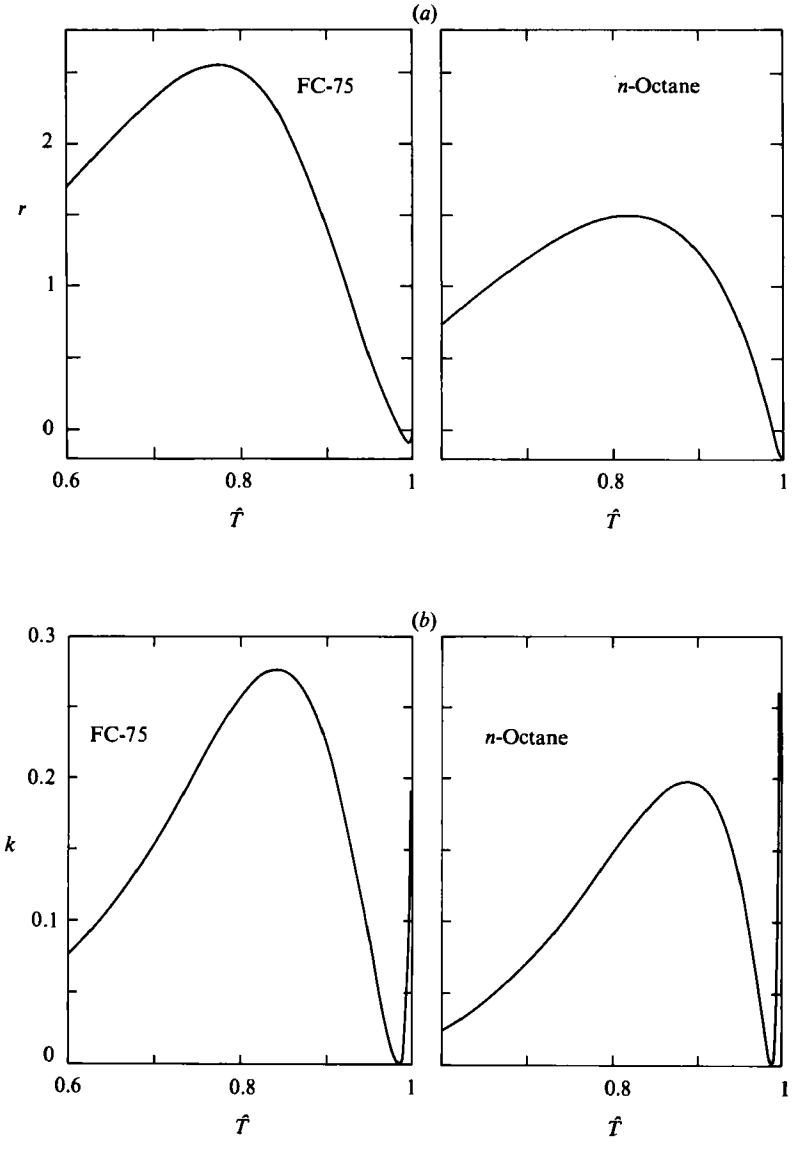

FIGURE 7. (*a*) Plot of the retrogradicity $r(T)$ for FC-75 and *n*-Octane. (*b*) Plot of the kink $k(T)$ for FC-75 and *n*-Octane.

	r			k		
Substance	$\hat{T}=0.6$	$\hat{T}=0.8$	$r_{max}(\hat{T})$	$\hat{T}=0.6$	$\hat{T}=0.8$	$k_{max}(\hat{T})$
Argon	−0.708	−0.606	—	0.362	0.455	—
n-Octane	0.735	1.483	1.493 (0.82)	0.0245	0.146	0.197 (0.89)
FC-75	1.697	2.517	2.55 (0.78)	0.0752	0.254	0.275 (0.85)

TABLE 2. Values of the retrogradicity $r(T)$ and the kink $k(T)$ on the saturated-vapour boundary. Given values of r_{max} and k_{max} lie in the region $\hat{T}_A > \hat{T} > \hat{T}_B$ (see figure 2)

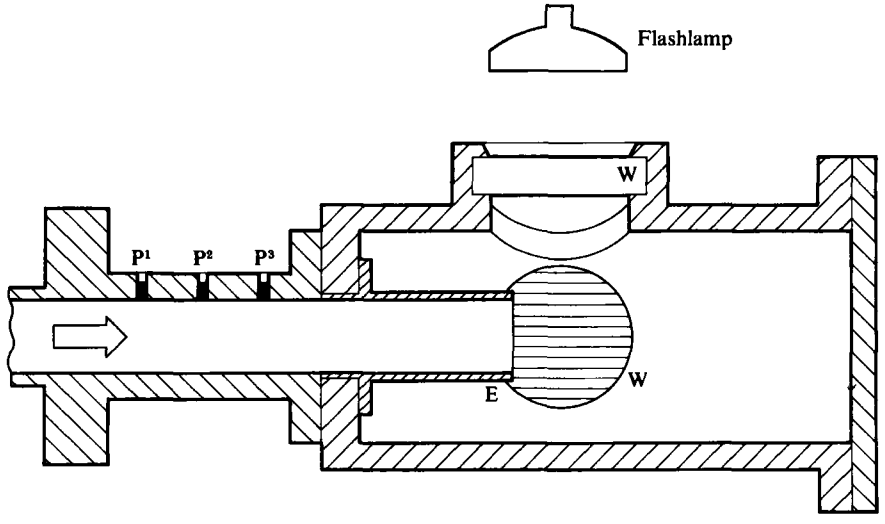

FIGURE 8. Observation chamber mounted at the end of the test section of the Rensselaer shock tube. Pressure transducers are P^1, P^2 and P^3. W = window (with background grid shown in the vertical window). E = end of the constant-diameter test section. The arrow indicates both the shock propagation and the flow direction.

shocks were produced mainly by reflection of the incident shock at the closed end of the test section. By virtue of the large density jump, this reflected shock propagates very slowly away from the closed end and is thus conveniently localized for observation. In the experiments reported here, performed at Rensselaer, the closed end is replaced by an open end, followed by a large-diameter, closed observation chamber (figure 8). The observed flow is thus a discharge emerging from a tube, a transient flow headed by a shock wave. This arrangement provides a rich, coherent variety of shock and phase-change phenomena.

The shock tube at Rensselaer has been described by Thompson *et al.* (1984). It is heated to an initial test temperature T_0 in the range 80–170 °C: for the test fluids used, this allows an initial test pressure $P_0 > P_\sigma(T_0)$ in the range 0.1–8 bar. The superheated test vapour has a correspondingly high density, which is useful for the refractive technique of flow visualization (Thompson, Kim & Meier 1985). The low-pressure regime is not yet explored.

The shock-tube inside diameter is 57.6 mm ($R = 28.8$ mm), the driver section is 3.50 m long and the test section is 1.67 m long, measured from the diaphragm to the open end. Three Kistler dynamic pressure transducers type 603B are located 306, 256, and 206 mm from the open end of the test section. The shock tube, including the observation chamber, is wound with electrical resistance heating and covered with ceramic-fibre insulation. With this arrangement, initial test temperatures can be maintained to within ± 2 °C. Pressure burst of the diaphragms is achieved by releasing nitrogen driver gas from the gas bottle. Burst pressures ΔP between 1 and 40 bars can be selected, using various combinations of diaphragm films. Initial temperature T_0 and pressure P_0 within the test section and observation chamber are measured with a thermocouple and a strain-gauge pressure transducer respectively. Transient data from the three pressure transducers and from a photodiode registering the flashlamp are stored in a digital transient recorder. The shock signal at the first pressure transducer is used as an initiating signal.

Property	Substance			
	FC-75	PP3	*n*-Octane	PP1
Formula	$C_8F_{16}O$	C_8F_{16}	n-C_8H_{18}	n-C_6F_{14}
Molecular weight M	416.06	400.06	114.23	338.04
Boiling point (K)	375.8	374.65	398.82	330.31
Critical temperature T_c(K)	500.21	514.65	568.76	447.7
Critical pressure P_c(bar)	16.07	18.81	24.87	19.0
Critical volume v_c(cm^3/g)	1.70	1.52	4.31	1.64
Acentric factor ω	0.55	0.472	0.394	0.483
$\tilde{c}_v = c_v^\circ(T_c)/R$	53.4	53.9	36.8	40.5

TABLE 3. Properties of some retrograde substances

Because the retrograde test gases have high molecular weights, the density of the test fluid at the contact surface in the shock-tube flow is greater than that of the driver gas. Typical initial density ratios across the intact diaphragm are ≈ 10; after diaphragm burst, this ratio increases to ≈ 100, by virtue of driver-gas expansion and test-fluid compression. To avoid a suspected Rayleigh–Taylor instability, a light balsawood piston was placed ahead of the diaphragm in many experiments, effectively replacing the contact surface.

The experimental events reported here took place in the observation chamber (175 mm diameter × 406 mm long), where the shock system emerges from the open end of the test section. Visibility of the flow in the photographs taken through the observation-chamber window depends upon either condensation, or refraction of the grid lines on a sheet mounted against the cylindrical inner surface of the chamber.

The primary test fluid is a proprietary fluorocarbon, designated FC-75 and based on perfluoro-Tetrahydrobutylfuran, $C_8F_{16}O$. The secondary test fluid is also a proprietary fluorocarbon, designated PP3 and based on perfluoro-1,3-Dimethyl-cyclohexane, C_8F_{16}: it was used only in the shock stability experiments. Properties of both test fluids are given in table 3.

4. Computational models

The flow observed in the shock-tube observation chamber is coupled with the emergence of a liquefaction shock wave from the tube: thus, we are dealing with an unsteady compressible flow with shock waves and visible phase changes (figure 9). This complex flow has many features in common with other flows in which fluid is impulsively set into motion, in ideal gases and even in liquids. The experimental flow shows several features for which a model is desirable, including the liquefaction shock, shock splitting into a single-phase forerunner shock and a following condensation discontinuity, rarefaction shock and a rich flow-field structure which includes a large ring vortex and additional shock waves. The computational models used are the following.

4.1. *Jump conditions at gasdynamic discontinuities*

The Rankine–Hugoniot equation has the alternative forms

$$[h] = \tfrac{1}{2}(v_1+v_2)[P]; \quad [e] = -\tfrac{1}{2}(P_1+P_2)[v]; \tag{18}$$

where the square brackets indicate a jump, e.g. $[P] = P_2 - P_1$. In every case treated, at least one of the two states (upstream, downstream) is an equilibrium state.

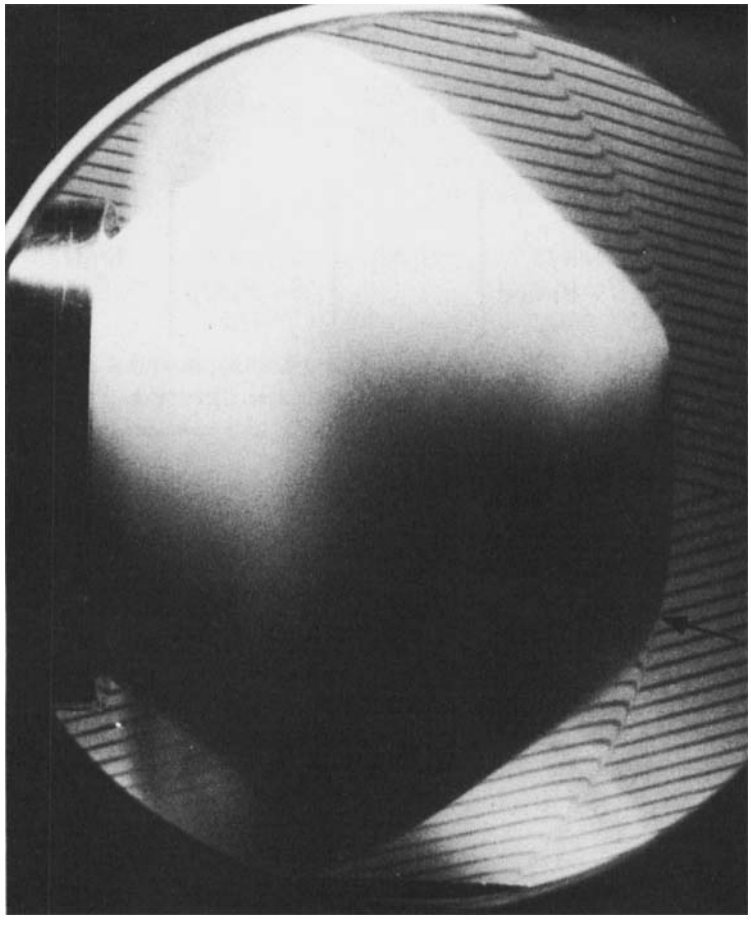

FIGURE 9. Emergence of the liquefaction shock from the open end of the shock-tube test section into the observation chamber. Flow is from left to right. A curved, vapour-phase forerunner shock and a condensation discontinuity have split off from the normal liquefaction shock at the triple point (indicated by the arrow). Initial conditions $P_0 = 0.726$ bar, $T_0 = 100$ °C. Shock Mach number $M_0 = 1.88$.

For shock-tube experiments in which the forerunner-shock velocity is measured, it is convenient to use real-gas series (Thompson 1983) for the calculation of the downstream state, which is typically supersaturated vapour. For a shock Mach number M_0, the non-dimensional pressure jump Π and temperature jump $[T]$ can be found from

$$\Pi = \frac{1}{\Gamma}(M_0^2-1) - \frac{1}{6\Gamma^2}(G+2-2\Gamma)(M_0^2-1)^2 \ldots, \tag{19}$$

$$\frac{[T]}{T_0} = GH + \tfrac{1}{2}G(G+2-2\Gamma)\,H^2 \ldots, \tag{20}$$

where $\Pi = [P]/\rho_0 c_0^2$, $H = [h]/c_0^2 = \Pi(1-\Pi/2M_0^2)$, G is the Grueneisen parameter and Γ is defined in (17). For typical experimental conditions, this series technique is limited to forerunner shock Mach numbers less than about two.

4.2. *Numerical solutions of the inviscid equations of motion*

For unsteady flow, the Euler equations can be written in conservative form as

$$\frac{\partial \boldsymbol{M}}{\partial \tau}+\frac{\partial \boldsymbol{F}(\boldsymbol{M})}{\partial \hat{X}}+\frac{\partial \boldsymbol{G}(\boldsymbol{M})}{\partial \hat{Y}}+\boldsymbol{W}(\boldsymbol{M})=0, \tag{21}$$

where

$$\boldsymbol{M}=\begin{bmatrix}\hat{\rho}\\ \hat{m}\\ \hat{n}\\ \hat{E}\\ \hat{S}\end{bmatrix},\quad \boldsymbol{F}(\boldsymbol{M})=\begin{bmatrix}\hat{m}\\ \hat{m}^2/\hat{\rho}+\hat{P}\\ \hat{m}\hat{n}/\hat{\rho}\\ (\hat{E}+\hat{P})\hat{m}/\hat{\rho}\\ \hat{S}\hat{m}/\hat{\rho}\end{bmatrix},\quad \boldsymbol{G}(\boldsymbol{M})=\begin{bmatrix}\hat{n}\\ \hat{m}\hat{n}/\hat{\rho}\\ \hat{n}^2/\hat{\rho}+\hat{P}\\ (\hat{E}+\hat{P})\hat{n}/\hat{\rho}\\ \hat{S}\hat{n}/\hat{\rho}\end{bmatrix},\quad \boldsymbol{W}(\boldsymbol{M})=\frac{\epsilon\hat{n}}{\hat{y}}\begin{bmatrix}1\\ \hat{m}/\hat{\rho}\\ \hat{n}/\hat{\rho}\\ (\hat{E}+\hat{P})/\hat{\rho}\\ \hat{S}/\hat{\rho}\end{bmatrix}$$

In these equations, $\hat{\rho}$ is the density and $\hat{P}$ is the pressure; $\hat{m}$ and $\hat{n}$ are the momentum components in the axial direction $\hat{X}$, and the radial direction $\hat{Y}$ respectively; $\hat{E}$ is the total energy per unit volume and is related to the specific internal energy $\hat{e}$ by the expression

$$\hat{e}=\left(\frac{\hat{E}}{\hat{\rho}}-\frac{\hat{m}^2+\hat{n}^2}{2\hat{\rho}^2}\right), \tag{22}$$

ϵ is zero for planar flow and unity for axisymmetric flow.

The last of equations (21) is a species equation where $\hat{S}$ represents the mass concentration of one of the species. The calculations to be presented below are for a single chemical species but by including this equation the 'contact surface' bounding the set of particles initially in the shock tube can be identified as it is convected downstream by the flow field. The solution of the first four equations evolves independently of the fifth in this case.

The variables have been non-dimensionalized with respect to the critical state ρ_c, P_c and a length L. Thus, $\hat{\rho}=\rho/\rho_c$, $\hat{m}=m/(\rho_c P_c)^{\frac{1}{2}}$, $\hat{n}=n/(\rho_c P_c)^{\frac{1}{2}}$, $\hat{E}=E/P_c$, $\hat{e}=e/(P_c/\rho_c)$, $\hat{P}=P/P_c$, $\hat{S}=S/\rho_c$, $\hat{X}=X/L$, $\hat{Y}=Y/L$ and $\tau=t(P_c/\rho_c)^{\frac{1}{2}}/L$ (the length L will be the tube radius R).

The van der Waals equation of state and a constant specific heat c_v were used to relate the pressure to the state variables ρ and e. For single-phase states

$$\hat{P}=\frac{8\hat{\rho}\hat{T}}{3-\hat{\rho}}-3\hat{\rho}^2,\quad \hat{e}=\frac{\hat{c}_v\hat{T}}{Z_c}-3\hat{\rho},\quad \hat{s}=\hat{c}_v\ln\hat{T}+\ln\left(\frac{3}{\hat{\rho}}-1\right), \tag{23}$$

where $\hat{T}=T/T_c$ is the temperature, $\hat{s}=s/R$ is the entropy and $\hat{c}_v=c_v/R$. The critical compressibility factor is $Z_c=P_c/(R\rho_c T_c)=\frac{3}{8}$ for this state equation. The integration constants in the expressions for $\hat{e}$ and $\hat{s}$ were set equal to zero.

The sound speed, $\hat{c}=c/(P_c/\rho_c)^{\frac{1}{2}}$ was calculated using the thermodynamic identity

$$\hat{c}^2=\left(\frac{\partial\hat{P}}{\partial\hat{\rho}}\right)_{\hat{T}}+\frac{Z_c\hat{T}}{\hat{c}_v\hat{\rho}^2}\left(\frac{\partial\hat{P}}{\partial\hat{T}}\right)^2_{\hat{\rho}}. \tag{24}$$

In the two-phase region the following saturation-property descriptions of Barieau (1966) were used:

$$\frac{3(\hat{\rho}_l-\hat{\rho}_v)(6-\hat{\rho}_v-\hat{\rho}_l)}{(3-\hat{\rho}_v)(3-\hat{\rho}_l)(\hat{\rho}_v+\hat{\rho}_l)}=\ln\frac{\hat{\rho}_l(3-\hat{\rho}_v)}{\hat{\rho}_v(3-\hat{\rho}_l)},$$

$$\hat{T}_\sigma=\tfrac{1}{8}(3-\hat{\rho}_v)(3-\hat{\rho}_l)(\hat{\rho}_v+\hat{\rho}_l),\quad \hat{P}_\sigma=\hat{\rho}_v\hat{\rho}_l(3-\hat{\rho}_v-\hat{\rho}_l),$$

$$\hat{\rho}'_v=\frac{\hat{\rho}_v(3-\hat{\rho}_v)}{\hat{T}_\sigma(3-2\hat{\rho}_v-\hat{\rho}_l)},\quad \hat{\rho}'_l=\frac{\hat{\rho}_l(3-\hat{\rho}_l)}{\hat{T}_\sigma(3-\hat{\rho}_v-2\hat{\rho}_l)},\quad \hat{P}'_\sigma=\frac{\hat{\rho}_v\hat{\rho}_l(6-\hat{\rho}_v-\hat{\rho}_l)}{\hat{T}_\sigma}.$$

The subscript σ refers to the saturation boundary as before; $\hat{\rho}_v$, $\hat{\rho}_l$ are the reduced vapour and liquid densities respectively, on this boundary. The prime denotes differentiation with respect to reduced temperature. For a mixture,

$$\frac{1}{\hat{\rho}} = \frac{1-x}{\hat{\rho}_l} + \frac{x}{\hat{\rho}_v} \quad \text{or} \quad x = \frac{\hat{\rho}_v(\hat{\rho}_l - \hat{\rho})}{\hat{\rho}(\hat{\rho}_l - \hat{\rho}_v)}, \tag{25}$$

$$\hat{e} = (1-x)\,\hat{e}_l + x\hat{e}_v = \frac{\hat{c}_v \hat{T}_\sigma}{Z_c} - 3\left(\hat{\rho}_l + \hat{\rho}_v - \frac{\hat{\rho}_l \hat{\rho}_v}{\hat{\rho}}\right), \tag{26}$$

$$\hat{s} = (1-x)\,\hat{s}_l + x\hat{s}_v = \hat{c}_v \ln \hat{T}_\sigma + (1-x)\ln\left(\frac{3}{\hat{\rho}_l} - 1\right) + x \ln\left(\frac{3}{\hat{\rho}_v} - 1\right), \tag{27}$$

where x is the mixture quality. Using the definition $c_v \equiv (\partial e/\partial T)_\rho$ and (26) the mixture specific heat is

$$\hat{c}_{vm} = \hat{c}_v - 3Z_c\left[\hat{\rho}_l' + \hat{\rho}_v' - \frac{\hat{\rho}_l'\hat{\rho}_v + \hat{\rho}_v'\hat{\rho}_l}{\hat{\rho}}\right]. \tag{28}$$

The mixture sound speed was evaluated from (24) with the first term set equal to zero since pressure depends only on temperature in the two-phase region. The result is, for the van der Waals equation,

$$\hat{c}^2 = \frac{Z_c T_\sigma}{\hat{c}_v}\left(\frac{\hat{P}_\sigma'}{\hat{\rho}}\right)^2.$$

The conservation equations were solved using the shock-capturing, finite-difference scheme of Harten (1983). The jump conditions implicit in the Euler equations are inherently satisfied and shocks are formed automatically in the calculation. The algorithm is described for a perfect-gas flow by Yee, Warming & Harten (1982, 1983). Carofano (1984) worked out the details for a more general equation of state.

The calculation was started with a planar shock advancing down the tube; the initial data were obtained from the Rankine–Hugoniot jump conditions and equation of the state. Boundary conditions and the two-dimensional grid are discussed by Carofano (1984).

4.3. *Equations of state*

For calculation of the Rankine–Hugoniot jump conditions at shock and condensation discontinuities, the two-term virial equation (Tsonopoulos 1974), modified Benedict–Webb–Rubin or 'BWR 44' equation (Yamada 1973) and an extended virial equation due to Hobbs (1983) were used. Most of the data reduction was performed with the BWR equation. The equilibrium two-phase sound speeds were calculated from the BWR equation using formulations from Bursik & Hall (1981).

The use of the self-consistent van der Waals equation in the numerical solutions of the inviscid equations of motion means that those results must be considered semi-quantitative when the fluid deviates from an ideal-gas state.

5. Basic features of the emerging flow in the observation chamber

5.1. *General features*

The condensing flows considered in this paper are headed by a single liquefaction shock. As this shock emerges from the shock tube, the shock front and following flow become three dimensional as shown in figure 9. A number of observed effects require only that the fluid be compressible and are thus, to a large extent, independent of

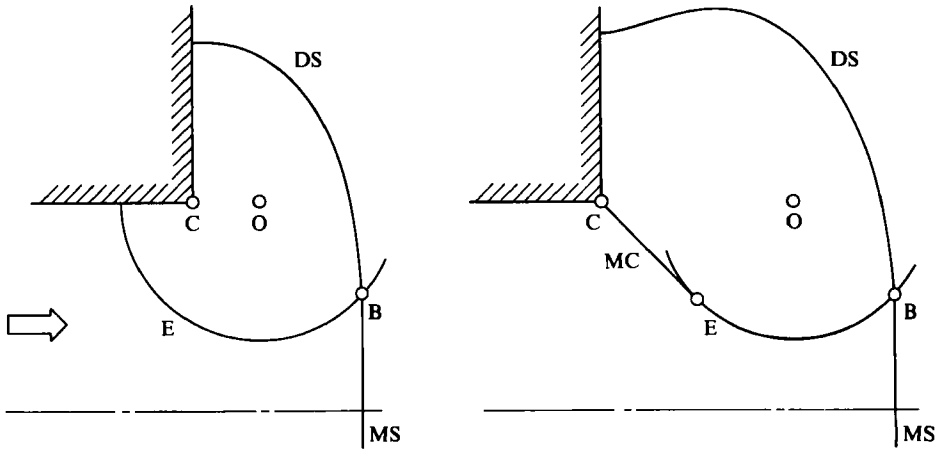

FIGURE 10. Mach construction, showing the first-signal expansion front E which originates when the plane main shock MS reaches the tube corner C. The diffracted shockfront is labelled DS. The expansion front E is centred on point O, originating at the corner C and convected with the (undisturbed) flow behind the shockfront MS. (*a*) Subsonic flow in the laboratory frame, $u_2 < c_2$; (*b*) Supersonic flow in the laboratory frame, resulting in a 'Mach-trumpet' configuration: MC = Mach cone.

the test fluid: the formation of a large ring vortex (visible in cross-section as hollow rings near the end of the shock tube in figure 9) is even similar to that observed in essentially incompressible fluids which are impulsively set into motion (Maxworthy 1977; Didden 1979). We begin by describing the general features of the emerging flow for a compressible fluid.

The basic motion in the laboratory frame can be understood as an outward flow of the compressed fluid from the tube, toward the right in figure 9, and expanding radially. The main shock advances to the right faster than the following fluid and continually sets 'new' fluid into motion behind it. The radial expansion of the flow from the tube can be understood with the help of a Mach construction similar to that given by Skews (1967*a*, *b*) and illustrated in figure 10. The construction differs according to whether the flow behind the shock front is subsonic or supersonic (in our experiments with liquefaction shocks, the supersonic case is usual, mainly because the two-phase mixture sound speed c_2 is small). That part of the region behind the main shock which has not yet been enveloped by the first signal expansion wave E remains undisturbed and thus preserves a uniform state, identical with the state inside the tube. Below point B, where the expansion wave intersects the main shock front, the shock is also undisturbed by the expansion and remains plane: until point B reaches the shock-tube axis, a diminishing portion of the shock front MS will thus remain plane.

The large ring vortex is generated by the rolling-up of the vortex sheet between the emerging jet of fluid and the initially stationary ambient fluid in the observation chamber. In common with the expansion front, the vortex thus originates at the tube corner C, where the flow separates. It is remarkable that the (inviscid) Euler calculations accurately represent the motion and growth of the vortex (compare Rizzi 1982).

For supersonic flow behind the main shock, the expansion front MC represents the

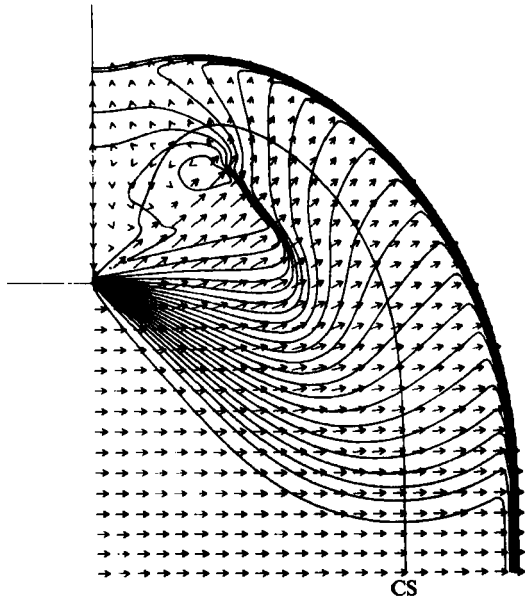

FIGURE 11. Emerging flow of a perfect gas ($\gamma = \frac{7}{5}$) from a tube, with shock Mach number $M_0 = 3$ and time $c_0 t/R = 0.49$, where R is the tube radius. Velocity vectors and contours of constant pressure are shown. CS = contact surface.

first characteristic of a quasi-steady Prandtl–Meyer expansion. With increasing time, the main shock and vortex ring move far downstream, the region in which the flow is quasi-steady grows and the flow tends toward a steady-state under-expanded nozzle discharge.

5.2. *Ideal-gas flows*

Discharge flows similar to that described here have been treated in the experiments of Payman & Shepherd (1946), Elder & de Haas (1952) and Skews (1967*a*, *b*), all of which involved ideal (or nearly ideal) gases. Comparison of these experiments, our calculations and our experiments show broad similarities, especially in the internal shock structure and the flow development with time. In the following, we describe calculations and certain experimental results for a perfect gas, i.e. an ideal gas with constant heat capacity.

Figure 11 shows the axisymmetric flow emerging from the tube, calculated for a flanged boundary in the exit plane of the nozzle. The 'Mach-trumpet' structure of figure 10(*b*) can be seen here as the first contour of constant pressure. The centre of the ring vortex can be located within the small, almost circular region and by the circulation apparent from the velocity vectors. A vortex-associated shock wave has been formed. The continuous line CS is a contact surface, made up of the fluid particles which were initially located in the tube-exit plane: the surface can thus be thought of as a balloon of unlimited extensibility, originally located in the exit plane.

The diffraction of a plane shock front around a right-angle corner (or a sharp corner of arbitrary angle) is the plane-flow analogue of the axisymmetric flow emerging from a tube. The plane diffraction is illustrated in figure 12. Instructive shadowgraphs by Oertel and Schardin are in Van Dyke (1982) and the papers of Skews (1967*a*, *b*). This flow, sometimes referred to as 'shock diffraction over a backward-facing step' remains self-similar (with similarity variables $X/c_0 t$ and $Y/c_0 t$, the origin of co-

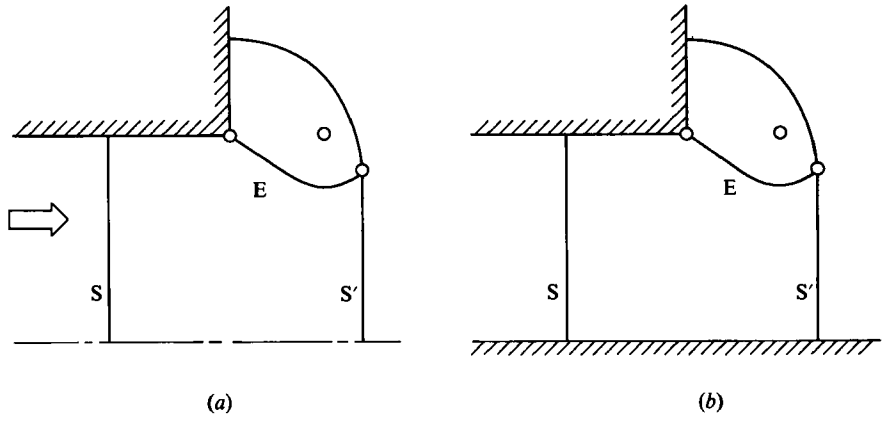

(a) (b)

FIGURE 12. Diffraction of an emerging shock front with supersonic flow behind the shockfront. S and S′ represent the positions of the shock front before and after emergence from the tube respectively. E is the expansion front. (*a*) Axisymmetric flow from a tube. (*b*) Plane, self-similar flow.

ordinates being at the corner) until the expansion front E reaches a lower boundary L: that is the flow field changes in size, but not in form, with increasing time. It is convenient to use this basically simple flow field to test the inviscid-flow computational model already described: as shown in figure 13 (*a*), the experimental results of Skews compare well with the computation (Carofano 1984).

The lines of constant entropy (isentropes) shown in figure 13 (*b*) have a conceptual relation to the vortex ring roll-up. Although the isentropes are neither streamlines nor path lines nor streak lines (see Batchelor 1967 for definitions), the isentropes of the corresponding *transformed* stationary flow (Jones, Martin & Thornhill 1959) are streamlines, geometrically identical with the isentropes in figure 13 (*b*). It is interesting that the local entropy maximum (small ellipsoidal contour enclosing the diamond symbol) corresponds exactly to the vortex core position measured by Skews from shadowgraphs.

With increasing time, the emerging perfect-gas flow shown in figure 11 tends toward the steady discharge from an 'underexpanded' nozzle, assuming that a quasi-steady flow from the shock-tube test section is maintained. The computed development of the flow with time is illustrated in figure 14. An increasing region of steady flow is left behind the advancing vortex ring: in the case illustrated, the vortex advances with an axial velocity $u_v \sim 0.7\, c_0$, where c_0 is the speed of sound ahead of the main shock. In the experiments reported here, however, the long observation times $c_0 t/R$ shown in figure 14 are not available. The observation time t_w limited by the diameter of the window is

$$\frac{c_0 t_w}{R} \approx \frac{2R_w}{M_0 R} \sim 1,$$

where R_w is the radius of the observation-chamber window and R is the tube radius. The duration of a quasi-steady outflow from the shock-tube test section is determined by the time of arrival t_{cs} of the contact surface (or the piston), which depends in turn on the length L_{ts} of the test section and the density ratio ρ_2/ρ_0 across the main shock:

$$\frac{c_0 t_{cs}}{R} < \frac{L_{ts}}{M_0 R(\rho_2/\rho_0)} \sim 1.$$

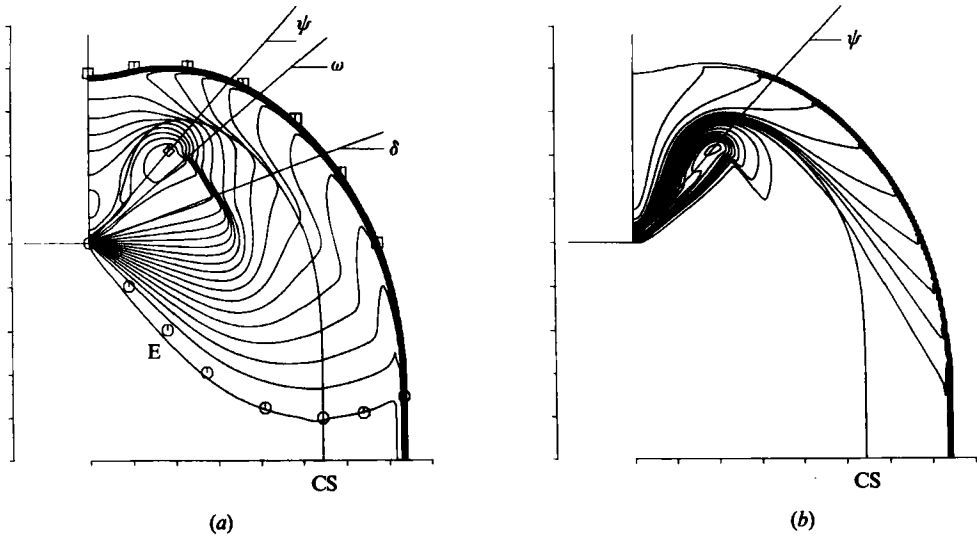

FIGURE 13. Self-similar, plane-flow shock diffraction around a right-angle corner for a perfect gas with $\gamma = \frac{7}{5}$, shock Mach number $M_0 = 3$. (*a*) Comparison of the inviscid flow calculation with experimental results of Skews: δ = 'terminator' angle (20°) of the low-pressure Prandtl–Meyer expansion characteristic, ω = 'slipstream' angle (40°) of the contact surface, ψ = vortex angle (48°). Constant-pressure contours are shown. The positions of the calculated expansion front E and the main shockfront agree with the experiments of Skews (indicated by data points). (*b*) Constant-entropy contours.

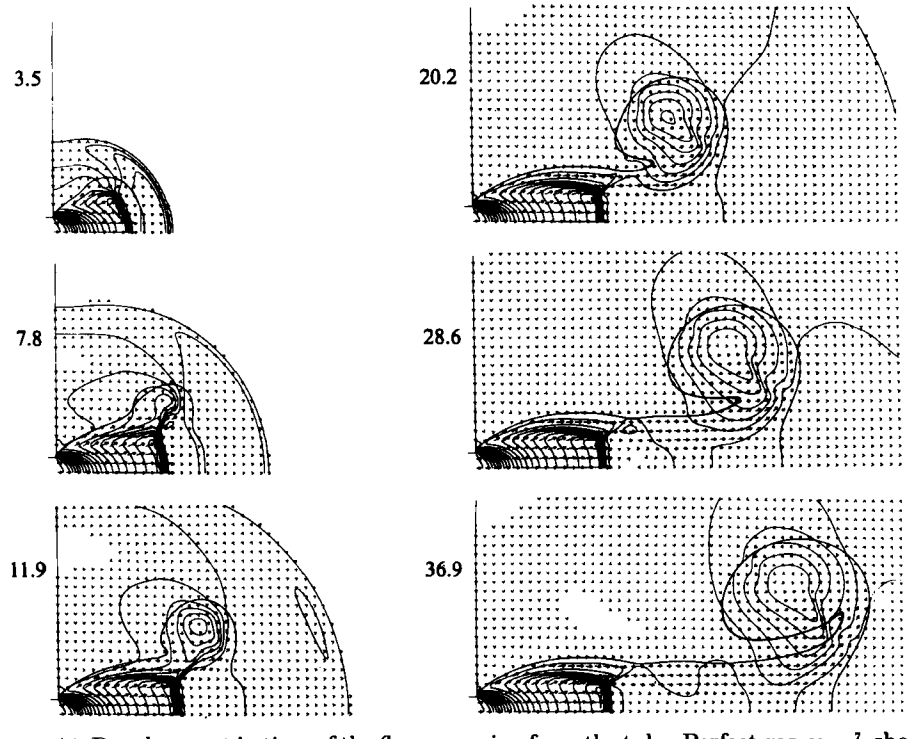

FIGURE 14. Development in time of the flow emerging from the tube. Perfect gas, $\gamma = \frac{7}{5}$, shock Mach number $M_0 = 3$. Pressure contours. The cell size for the numerical calculation is larger than that used for figure 11 by a factor of 20. Values of $c_0 t/R$ are shown.

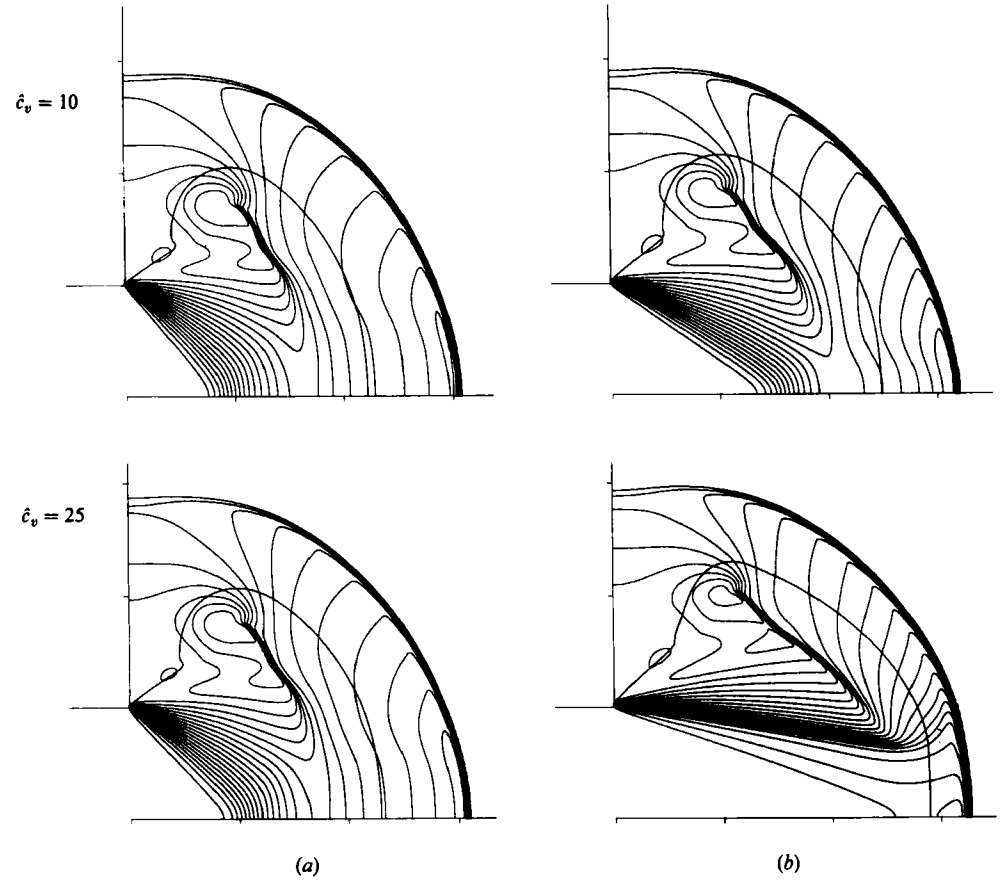

FIGURE 15. Computed flows emerging from the shock tube for two different heat capacities $\hat{c}_v$, with a shock Mach number $M_0 = 2$. (*a*) Perfect-gas shock structure at low reduced pressure. (*b*) Real-fluid shock structure at reduced pressure $P_0 = 0.275$ and reduced volume $v_0 = 7.75$. The fluid of higher heat capacity $\hat{c}_v = 25$ has developed a rarefaction shock in the expansion region, where several pressure contours coalesce. The non-dimensional time $c_0 t/R$ in each flow is approximately 1.1.

Depending on the actual case considered, the observable test time with a quasi-steady discharge may be limited by either t_w or t_{cs}.

5.3. *Aspects of real-gas flow*

Consistent with the emphasis of this work on multiatomic fluids of high molar heat capacity, it is of interest to examine the behaviour of the (still) single-phase gas flow with increasing heat capacity. The emerging flow, similar to that in figure 11, is shown for two constant heat capacities $\hat{c}_v = 10$ and $\hat{c}_v = 25$ ($\gamma^0 = 1.10$ and 1.04 respectively) in figure 15 for a fixed shock Mach number $M_0 = 2$. In the perfect-gas case, figure 15(*a*), ($P_0 \to 0$), the structure is qualitatively unchanged from that of figure 11. A similar statement applies to the real-gas case (figure 15*b*) with $\hat{c}_v = 10$. For the real-gas case $\hat{c}_v = 25$, however, the structure is qualitatively different: part of the *expansion* fan has steepened to form a rarefaction shock, which has the general form of the 'Mach trumpet' pictured in figure 10(*b*). The appearance of the rarefaction shock is associated with the existence of negative values of the fundamental derivative ($\Gamma < 0$), as mentioned in §2.

6. Mixture-evaporation shocks and related phenomena

The rarefaction shocks found in our experiments are of the mixture-evaporation type referred to in §§1 and 2. Their formation is associated with the discontinuity in equilibrium sound speed at the saturated-vapour boundary, i.e. the 'kink' k of (14), illustrated in figure 6. The upstream state for these shocks is liquid–vapour mixture, typically of low moisture, and the downstream state is superheated vapour.

The variety of possible rarefaction discontinuities in fluids is quite remarkable. An attempt at classification is offered in table 4. The various discontinuities have been observed or hypothesized. 'Discontinuity' is intended to mean an organized, macroscopic front that is in some sense thin. The classification and terminology are necessarily somewhat arbitrary and flows with chemical reaction (e.g. a flame front) are not included. All of the discontinuities listed involve a decrease in pressure and density across the front and most involve an increase in compressibility with increasing pressure, i.e. the Γ mechanism discussed in §2.

The following comments are numbered consistent with the entries in table 4. (i) The gas-phase rarefaction shock is the classical 'impossible' shock wave discussed in §5 and illustrated in figure 15(*b*) ($\hat{c}_v = 25$). Although it has never, to our knowledge, been observed, it almost certainly will be. (ii) The near-critical rarefaction shock recently reported by Borisov, Borisov & Kutateladze (1983) differs from (i) in that the requisite large value of c_v to achieve $\Gamma < 0$ is associated with near-critical power laws [$c_v \to \infty$ as $(T - T_c)^{-\alpha}$]. The upstream state must, apparently, be very near the critical point and the downstream state is in the mixture region. The measured thickness of the shock front is relatively large (≈ 5 cm) and is believed to be related to the large, near-critical correlation length. (iii) The mixture-evaporation rarefaction shock is the subject of this section and will be further discussed in the following. (iv) The liquid-evaporation deflagration is the subject of a future paper. (v) At the time of writing, a complete liquid-evaporation shock is hypothetical.

The three rarefaction shocks (i), (ii), (iii) are closely related, in that they depend on some form of $\Gamma < 0$ behaviour. They differ in that they occur in different states (regions of the (P, v)-plane, for example) and in that the required characteristic heat capacities $\tilde{c}_v$ differ greatly: only in a fluid with large $\tilde{c}_v$ would all three types of rarefaction shock be possible.

In the following, we confine ourselves to mixture–evaporation shocks. The calculated shock front shown in figure 16 has a typical 'Mach-trumpet' shape similar to that in figure 15(*b*) ($\hat{c}_v = 25$). The rarefaction shock forming the sides of the trumpet has developed by the nonlinear ($\Gamma < 0$) concentration of the distributed expansion waves. The main compression shock forms the front of the trumpet. Experimentally observed evaporation–rarefaction shocks are shown in figure 17.

The pressure range of the expansion at the shock-tube exit is of the order $P_2 - P_0$ and is typically large compared with the maximum possible pressure amplitude of the evaporation shock. In this situation, the evaporation-shock discontinuity is imbedded in an isentropic expansion and will evolve toward a double Chapman–Jouquet wave, or sonic–sonic shock, as discussed by Thompson & Lambrakis (1973) for the case of one-dimensional unsteady flow. The sonic–sonic solution is thus the natural limiting form, determined by the characteristic wave velocities, with the normal components of both the inflow and outflow being sonic, e.g. $M = M_{1n} = M_{2n} = 1$. The amplitude of the evaporation shock is a maximum in this case, as illustrated in the pressure–volume diagram of figure 18(*a*). The evolution of the limiting sonic–sonic solution is shown in figure 18(*b*).

Discontinuity	Phases	c_v required	Condition	Reference
(i) Gas-phase rarefaction shock	Vapour	Large	$\Gamma < 0$	Cramer & Kluwick (1984) Thompson & Lambrakis (1973) Zel'dovich (1946)
(ii) Near-critical rarefaction shock	Vapour / Mix	None	$\Gamma < 0$	Borisov, Borisov & Kutateladze (1983)
(iii) Mixture-evaporation rarefaction-shock	Mix / Vapour	Moderate	$r < 0$ ($\Gamma = -\infty$)	This work
(iv) Liquid-evaporation deflagration	Liquid / Mix	?	—	A future paper Chaves (1983)
(v) Complete liquid-evaporation shock	Liquid / Vapour	Large	—	Slemrod (1983, 1984)
(vi) Near-spinodal liquid-evaporation front	Liquid / Vapour	None	—	Shepherd & Sturtevant (1982)
(vii) Thermal evaporation front	Liquid / Vapour	None	Heat conduction	Knuth (1959)

TABLE 4. Rarefaction discontinuities in fluids

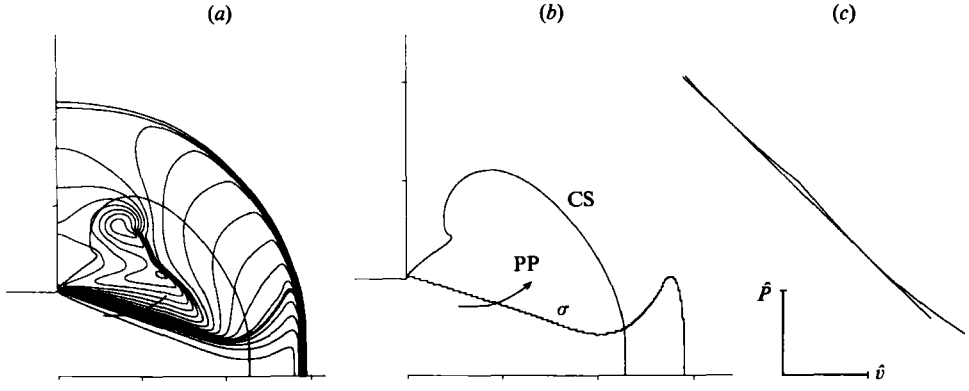

FIGURE 16. Computed evaporation-rarefaction shock with initial conditions $\hat{P}_0 = 0.275$, $\hat{v}_0 = 6.90$. The liquefaction-shock Mach number $M_0 = 1.45$ and $c_0 t/R = 1.43$. (*a*) Pressure contours showing the rarefaction shock, with a form similar to the 'Mach trumpet' in figures 10(*b*) and 11. (*b*) Contact surface CS, vapour saturation boundary σ and particle path PP. (*c*) Computed adiabet $P(v)$ along the particle path. The pressure bar corresponds to a reduced pressure change of 0.1; the volume bar corresponds to a reduced volume change of 1.

The appearance of this limiting solution in a three-dimensional flow was tested in the numerical calculation illustrated in figure 16. For the particle path selected, the flow is quasi-steady and the particle path corresponds to a streamline (the quasi-steady flow was confirmed by repeating the path and state calculation at later time with identical results). The fluid states along this path trace out the adiabat in figure 16(*c*).

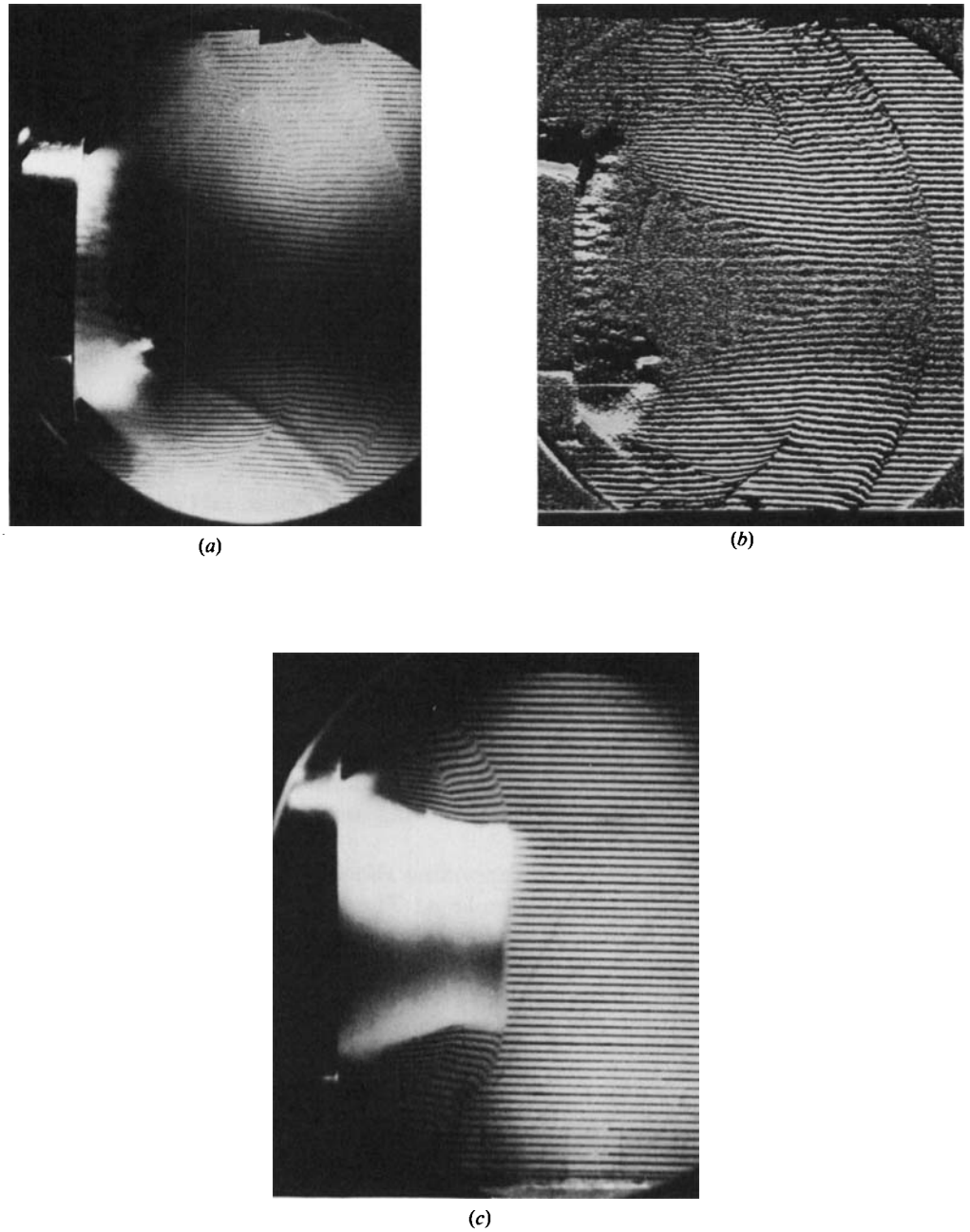

(*a*) (*b*) (*c*)

FIGURE 17. Experimental photographs of evaporation-rarefaction shocks. (*a*) Rarefaction shock with a low-moisture ($y \approx 6\,\%$) upstream state. Initial conditions $P_0 = 1.30$ bar, $T_0 = 160$ °C. Liquefaction-shock Mach number $M_0 = 2.31$ ($c_0 = 88.68$ m/s). (*b*) Processed image for the photograph shown in (*a*). (*c*) Rarefaction shock with a high-moisture ($y \approx 20\,\%$) upstream state. Initial conditions $P_0 = 1.50$ bar, $T_0 = 160$ °C. Liquefaction-shock Mach number $M_0 = 2.26$ ($c_0 = 87.99$ m/s).

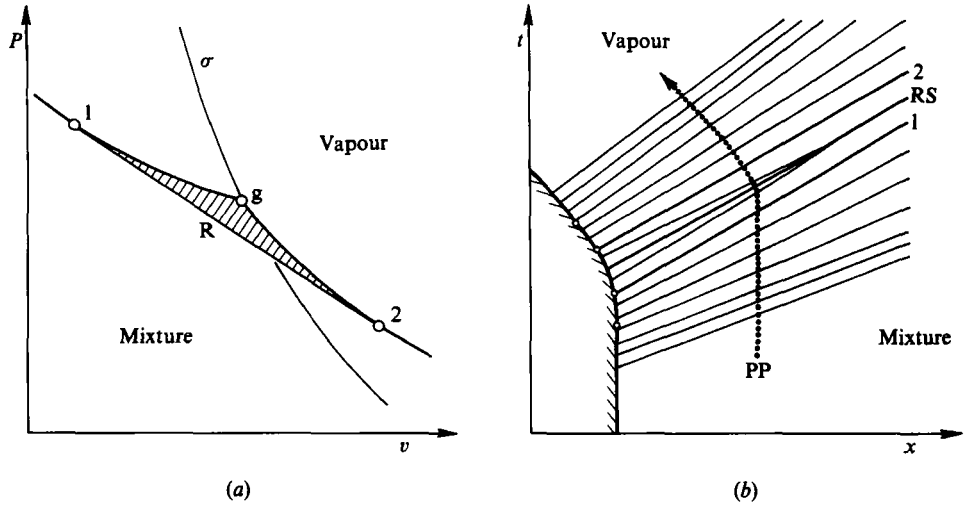

FIGURE 18. Double Chapman–Jouguet (sonic–sonic) evaporation shocks. (*a*) Construction of the sonic–sonic solution in the pressure–volume plane. The shaded area corresponds to the entropy jump $[s]$. R = Rayleigh line. (*b*) Development of the sonic–sonic shock in one-dimensional flow in an x–t wave diagram, corresponding to piston withdrawal (shaded line). The Chapman–Jouguet characteristics (1) and (2) are parallel, yielding the asymptotic sonic–sonic solution at $x = \infty$. PP = particle path, RS = rarefaction shock.

The shock is artificially broadened by numerical viscosity so it is difficult to determine its slope where it intersects the streamline. As a guide, the saturation boundary (figure 16*b*), which lies approximately midway through the shock transition region, can be used. A Chapman–Jouquet tangent construction then yields values for M_{1n} and M_{2n} of 1.016 and 0.986 respectively. The limiting sonic–sonic form thus appears to be approximately observed.

It is of interest to work out the corresponding shock amplitudes $[P]$, $[v]$ and $[s]$. The following estimates are based on figure 18 (*a*). The entropy jump across the shock is very small, so that it is possible to treat the shock adiabat 1–2 as an isentrope, with the discontinuity in slope at g given by the 'kink' $k(T)$. The curvature of the isentrope is fixed by the fundamental derivative Γ and the non-dimensional amplitudes are thus fixed by k and Γ. The calculation yields

$$-\frac{[P]}{\rho_g c_g^2} = \frac{k}{2\Gamma(k+1)} \tag{29}$$

$$\frac{[v]}{v_g} = [(\alpha-1)^{2\Gamma}(2\Gamma/k)]^{1/2\Gamma-1} \tag{30}$$

where $\alpha \equiv (k+1)^{1/2\Gamma}$ and the subscript g denotes the (vapour-phase) value at the saturation boundary σ. The entropy jump is fixed by the shaded area in figure 18 (*a*), according to the formula

$$\overline{T}[s] = \oint P \, dv, \tag{31}$$

where $\overline{T}$ is the average temperature along the adiabat 1–2, taken here to be T_g. This yields

$$\frac{\overline{T}[s]}{c_g^2} = \frac{k\epsilon^2}{6(k+1)}[1-\tfrac{2}{3}(\Gamma-1)\epsilon+\tfrac{1}{6}(\Gamma-1)(2\Gamma-3)\epsilon^2\ldots], \tag{32}$$

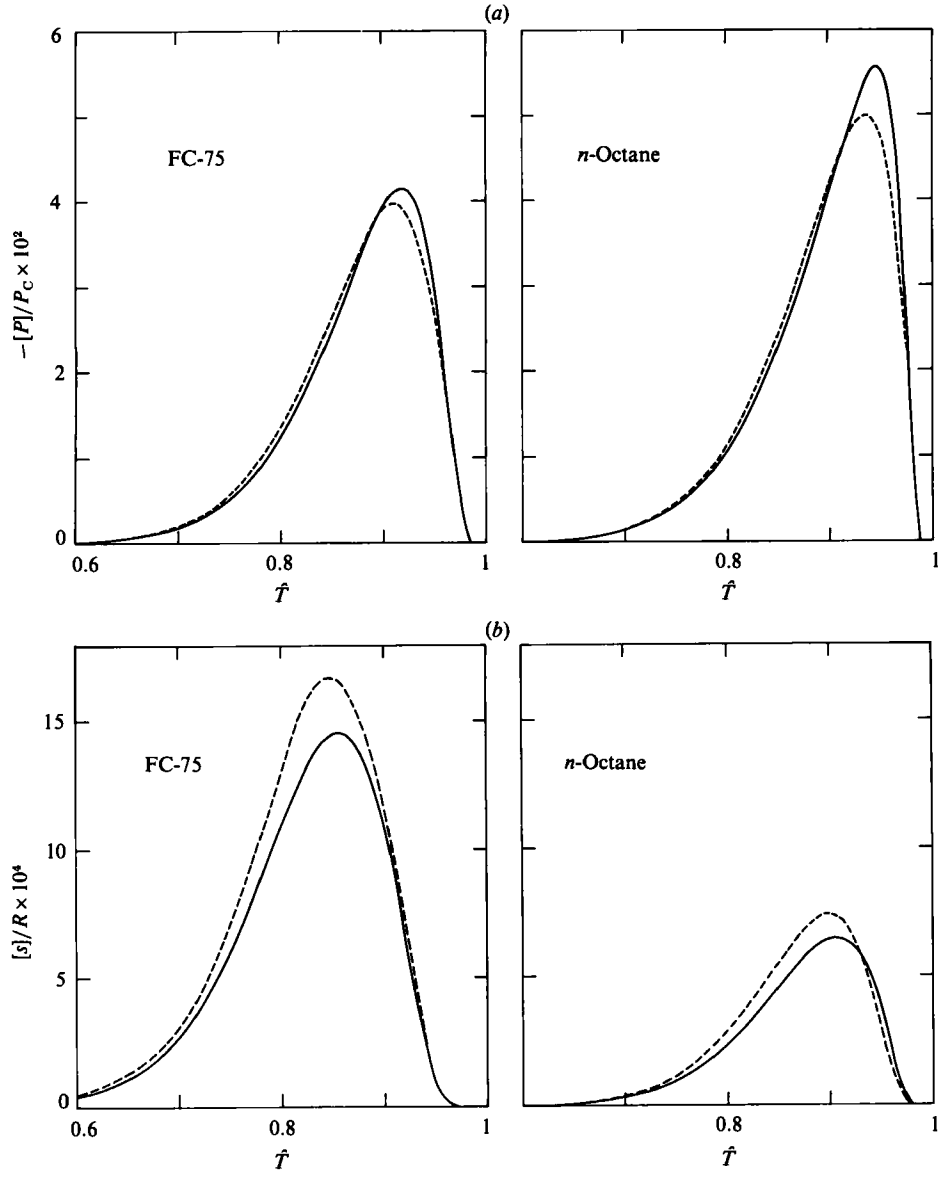

FIGURE 19. Pressure amplitude $[P]$ and entropy jump $[s]$ for sonic–sonic shocks as functions of reduced temperature $\hat{T}$. The continuous curves represent 'exact' calculations using the Hobbs equation of state, the dashed curves equations (29) and (32). (*a*) Pressure jump. (*b*) Entropy jump.

where the small parameter ϵ is given by

$$\epsilon \equiv 1-\frac{v_1}{v_g} = 1-\left[\frac{2\Gamma(\alpha-1)}{k}\right]^{1/2\Gamma}.$$

It can be shown that the left side of (32) is of order k^3/Γ^2. Comparisons of the above formulas with exact numerical calculations are shown in figure 19.

The limiting sonic–sonic form of the evaporation shock illustrated in figure 18 can be verified by the equality of the wave velocities $u+c$ for the two Chapman–Jouguet characteristics 1 and 2 (this simply means that both sides of the shock front propagate

with the same velocity). The method of characteristics for simple C^+ waves in an homentropic medium, i.e. neglecting the entropy jump across the shock, yields for the wave velocity W (see e.g. Thompson 1972)

$$W \equiv u+c = \int \frac{\Gamma \mathrm{d}P}{\rho c} + \text{const.} \tag{33}$$

It is convenient to rewrite this in terms of the acoustic impedance $g=\rho c = (-(\partial P/\partial v)_s)^{\frac{1}{2}}$ and the specific volume v,

$$W = \int v \, \mathrm{d}g + \text{const.} \tag{34}$$

For integration along an arbitrary S-shaped path $1 \rightarrow 2$, with tangency (sonic) conditions as in figure 18(*a*),

$$\overline{g^2} = \frac{1}{v_2-v_1}\int \left(\frac{\partial P}{\partial v}\right)_s \mathrm{d}v = -\frac{P_2-P_1}{v_2-v_1}. \tag{35}$$

The right-hand side is just the square of the mass flux through the shock: with the tangency conditions that the normal components of velocity relative to the shock front are sonic, this yields

$$\overline{g^2} = g_1^2 = g_2^2. \tag{36}$$

Integrating (34) by parts with $g_1 = g_2$ yields for the difference of the wave velocities

$$\frac{W_2-W_1}{v_2-v_1} = g_1 - \frac{1}{v_2-v_1}\int g \, \mathrm{d}v = g_1 - \bar{g}. \tag{37}$$

With (36), this can be written

$$\frac{W_2-W_1}{v_2-v_1} = \frac{\overline{g^2}-\bar{g}^2}{g_1+\bar{g}} \geqslant 0. \tag{38}$$

With $c^2 = v^2 g$, $g_1 \simeq \bar{g}$ and (30), this can be written

$$W_2 - W_1 \approx \frac{kc_g}{2\Gamma_g}\frac{\overline{g^2}-\bar{g}^2}{2g_1^2} \geqslant 0. \tag{39}$$

For $k = \frac{1}{5}$, $\Gamma_g = 1$ and $c_g = 80$ m/s, a numerical estimate yields $W_2 - W_1 \simeq 4$ mm/s: this small, positive value can be related to the entropy jump across the shock.

The above results implicitly require that $r > 0$, so that the isentrope enters the mixture region with increasing pressure. If $r < 0$ (regular fluid), a stable compression-evaporation shock is possible, but it would not have a limiting form comparable to the sonic–sonic shock.

Additional observations from our shock-tube experiments are briefly described here for completeness. These include shock splitting and measurements of the two-phase sound speed in the region behind the liquefaction shock.

Shock splitting can be seen in the experimental photograph of figure 9. This splitting occurs when the main liquefaction shock is weakened, e.g. by three-dimensional expansion, to the point where condensation behind the shock is no longer spontaneous and immediate. In this case, the condensation front falls behind, as a separate discontinuity, leaving a region of supersaturated vapour just behind the forerunner shock front. (Shock splitting will be described in detail in a following paper, with the title 'Wave Splitting in a Large-Heat-Capacity Fluid.')

Measurements of the liquid-vapour sound speed were made by photographic

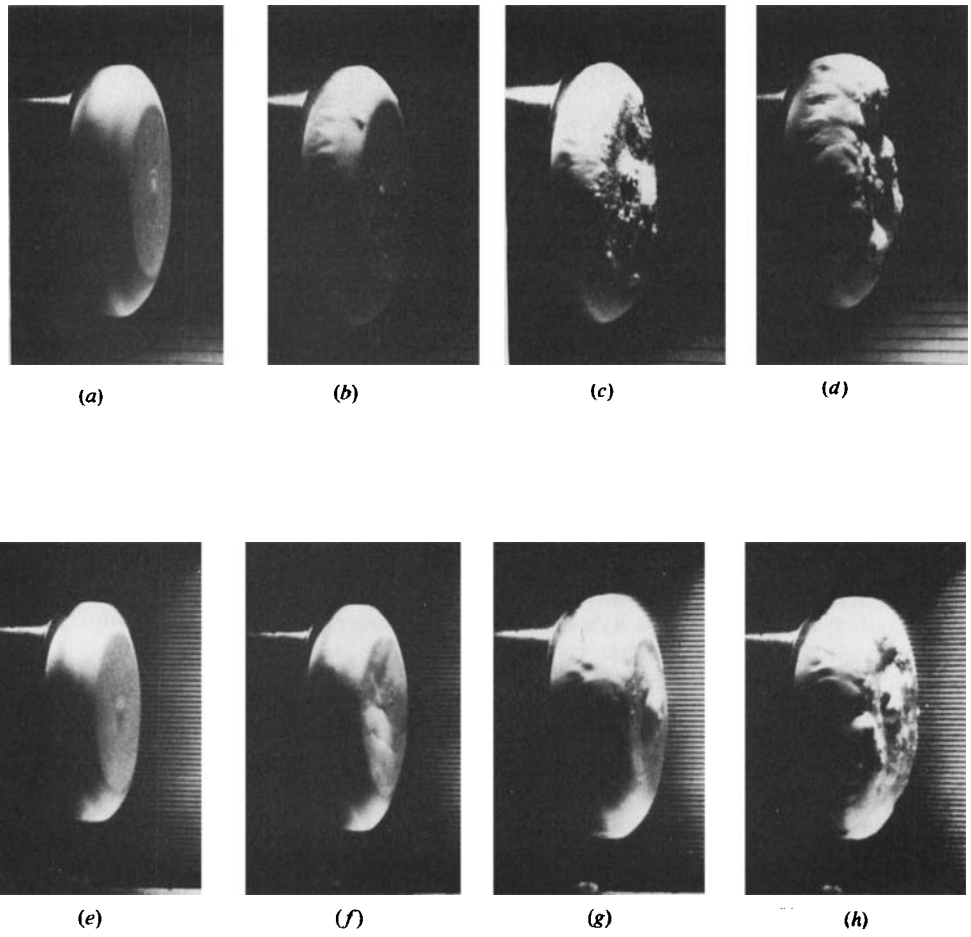

FIGURE 20. Transition from smooth to chaotic liquefaction shock fronts with increasing shock Mach number. The first row of photographs (*a–d*) shows shock fronts in FC-75 with $P_0 = 1.40$ bar, $T_0 = 120$ °C and $c_0 = 81.7$ m/s ahead of the shock front. The FC-75 experiments in this series were run with pistons. The second row of photographs (*e–h*) shows shock fronts in PP3 with $P_0 = 1.70$ bar, $T_0 = 130$ °C and $c_0 = 84.6$ m/s. The PP3 experiments in this series were run without pistons. The shock Mach numbers M_0 and computed moisture fractions are, respectively, for each experiment: (*a*) 2.10, ≈ 0.7; (*b*) 2.10, ≈ 0.7; (*c*) 2.17, ≈ 0.8; (*d*) 2.30, ≈ 0.9; (*e*) 2.22, ≈ 0.9; (*f*) 2.32, ≈ 1.0; (*g*) 2.31, ≈ 1.0; (*h*) 2.42, ≈ 1.0.

observation of the diameter defined by point B in figure 10 (Chen 1984). These measurements are pertinent to the discussion of liquefaction-shock-front stability in the following section.

7. Transition from smooth to chaotic liquefaction shockfronts

Over a range of initial conditions, transition from a smooth liquefaction shock front to a chaotic liquefaction is observed with increasing shock Mach number, as shown in figure 20. The smooth-to-chaotic transition, measured from the onset of visible small disturbances to the complete disappearance of shock front planarity, occurs over a relatively narrow range of the shock Mach numbers – although the irregularity of the shock front increases further at still higher shock Mach numbers. It is natural

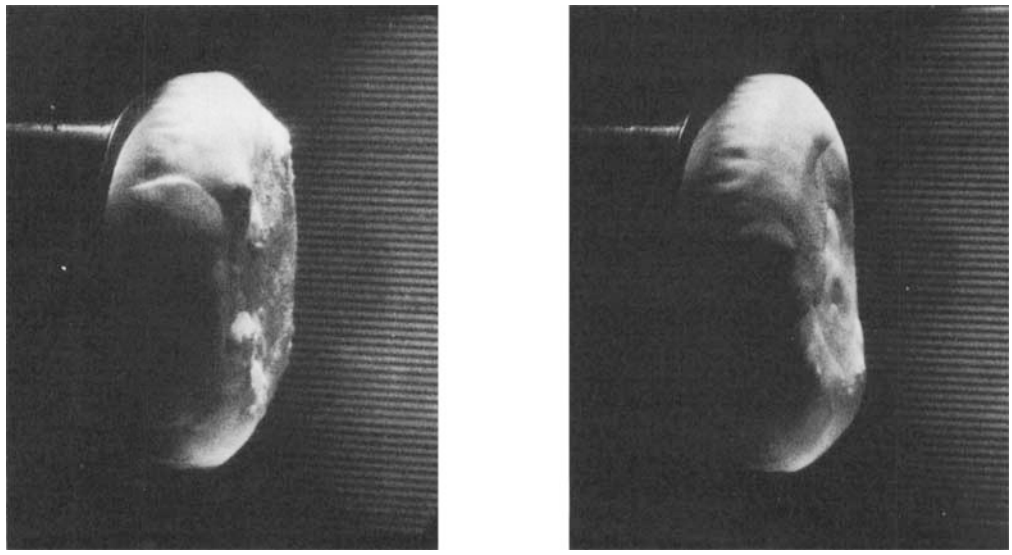

(a) (b)

FIGURE 21. Test for the effect of a driving piston on shock-front stability. Test fluid is PP3 with $P_0 = 1.70$ bar, $T_0 = 130$ °C and $c_0 = 84.6$ m/s. The shock Mach number $M_0 = 2.31$ in both cases. (*a*) With piston. (*b*) Without piston. Moisture fraction $y \approx 1$.

to describe this situation as a transition to turbulence (Thompson *et al.* 1984), the turbulent region being behind the irregular shock front.

The fluorocarbon test gas in which the chaotic shock fronts are observed is considerably more dense than the nitrogen driver gas (the density ratio is ≈ 100), so that the possibility of a Raleigh–Taylor instability exists at the shock-tube contact surface: in turn, such an incipient instability could conceivably drive the observed shock-front transition. To test for this possibility, a lightweight balsawood piston was placed on the test side of the diaphragm, thus effectively replacing the contact surface. Tests were run at identical initial conditions and shock Mach numbers with and without pistons (see figure 21). No discernible difference was found, suggesting that the observed instability is an inherent property of the shock transition, although downstream disturbances may have an effect on the structure.

The photograph in figure 22(*a*) of the chaotic liquefaction shock front inside the shock tube demonstrates that the observed transition is not associated with the expansion at the exit of the test section into the observation chamber.

A fascinating variety of surface features appears in the course of the smooth→chaotic transition. These include, in the approximate order of appearance with increasing shock Mach number: a small, regular protuberance or 'button' at the centre of the shock front (figure 20*a*); regular surface waves (figures 20*a* and 22*b*); small-scale surface asperities or eruptions (figures 20*b* and 22*d*); surface discontinuities resembling cracks or fractures (figures 20*f* and 22*e*); large-scale protuberances and rolls (figures 20*d* and 22*e*); fully chaotic shock fronts with a remarkable resemblance to cumulus clouds (figure 22*f*).

A remarkable form of instability in *complete* liquefaction shocks was found by Dettleff *et al.* (1979). Photographic observation through the clear-liquid phase downstream of the liquefaction shock front showed numerous and very small vortex rings which appeared to originate at or near the shock front itself. The stereoscopic

observations of Dettleff *et al.* (1982) showed that these vortex rings move *toward* the shock front in the frame of the liquid behind the shock, thus defining the sense of rotation of the toroidal rings: this rotation corresponds to a 'jet' through the vortex core in the direction of the shock front. These circumstances tend to support the hypothesis that the small-scale asperities on the shock front in our experiments (e.g. in figure 22*c*) correspond to the ring vortices, in this case seen from the other (upstream) side of the shock front as a surface eruption. A test of this hypothesis requires detailed experiments.

The liquefaction shocks observed by Dettleff *et al.* were produced by reflection of an incident shock at the closed end of the Goettingen shock tube. The liquefaction shock front and the fluid behind it are thus stabilized by the fixed endwall. The boundary conditions in the Rensselaer experiments are different: in the frame of the fluid behind the shock the 'fixed' endwall is formed by the piston face (say), but the shock-tube walls are moving at a velocity ≈ 200 m/s, leading to a complicated viscous flow.

Qualitative support for the shock-front instability reported here is provided by recent, preliminary experiments in Goettingen (Meier & Thompson 1985), in which small projectiles were fired through stationary PP1 test vapour ($P_0 = 1$ atm, $T_0 = T_\sigma = 57.2$ °C) at flight Mach numbers M_∞ of 1.76, 2.31, 4.41 and 4.87. At the lowest two values, the liquefaction bow shock is observed to be smooth, but at $M_\infty = 4.41$ and higher, it is choatic.

A theoretical basis for the observed shock-front instability may be provided by the stability analysis of Kontorovich (1957) as described by Fowles & Houwing (1984). The condition for stability is written in terms of the flow properties behind the shock front, with a Mach number M in the frame of the shock front (thus $M \leqslant 1$ for almost all shocks):

$$K \equiv (G+1)\left(\frac{v_0}{v}-1\right)M^2 < 1, \tag{40}$$

where $G = v(\partial P/\partial e)_v$ is the Grueneisen parameter and v_0/v is the density ratio across the shock. Thus, if $K > 1$, the possibility of an instability exists: in the analysis, the instability appears as 'steady transverse waves'. A sensitive and somewhat ambiguous parameter in (40) is the mixture sound speed appearing in the M^2 term. In figure 23, the value of K is plotted with increasing shock Mach number M_0 for fixed initial conditions, for three distinct sound speeds – namely the (in part extrapolated) experimental-mixture sound speed c_m, the calculated equilibrium sound speed c_i and the sound speed c_{dv} of dry saturated vapour at the mixture temperature. For the first two sound speeds, the Kontorovich parameter is well exceeded.

Credibility for the idea of a definite stability limit based on shock strength is lent by the observed persistence of stable oblique shock fronts, weaker than the main liquefaction shocks, for example, in figures 20(*b*), (*f*), and 22(*d*). The normal Mach number of these oblique shocks falls below the value of M_0 at which transition is observed (see figures 20 and 23).

The experiments described by Dettleff *et al.* (1979) showed large pressure fluctuations at the shock-tube endwall (i.e. behind the shock) in cases of complete liquefaction. The amplitude of these fluctuations varied considerably between experiments, as shown in figures 11, 12 and 27 of that paper. It is possible that the fluctuations correspond to shock-front instability in those experiments, although other hypotheses could be suggested. The wall-transducer pressure measurements in the experiments reported here appear to show a distinctive pressure signature in cases of chaotic shock fronts (Yoon 1985).

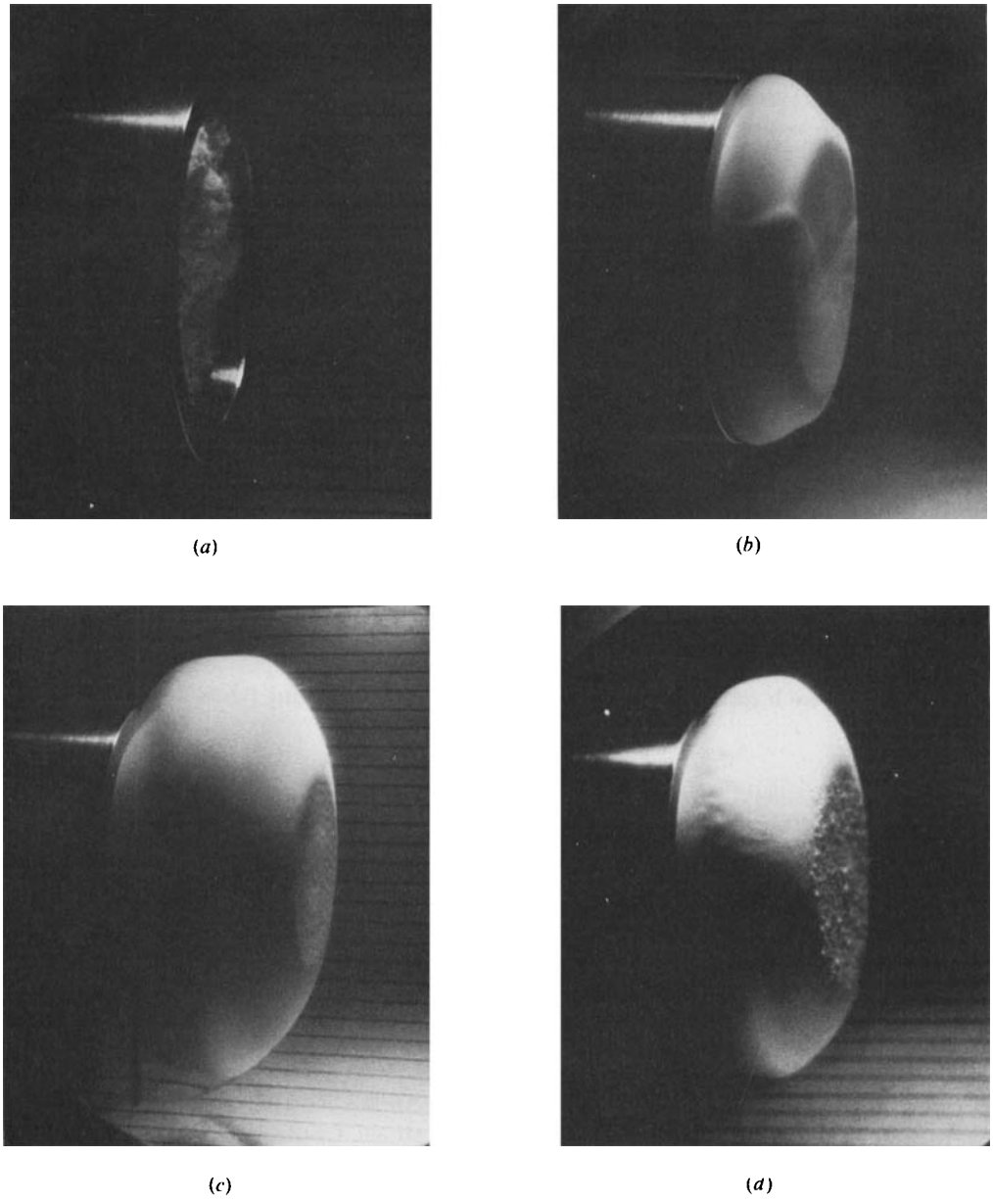

FIGURE 22. Various forms of irregularity observed on the shock-front surface in FC-75 experiments. Initial conditions $P_0 = 1.40$ bar, $T_0 = 120$ °C, $c_0 = 81.7$ m/s. (*a*) Photograph of a chaotic liquefaction shock front inside the shock tube, $M_0 = 2.39$, $y \approx 0.9$. (*b*) Regular surface waves, $M_0 = 1.64$, $y \approx 0.4$. (*c*) Complex surface waves, $M_0 = 2.10$, $y \approx 0.7$. (*d*) Small-scale surface asperities, $M_0 = 2.21$, $y \approx 0.8$. (*e*) Surface discontinuity resembling a crack or fracture and beginning larger protuberances, $M_0 = 2.20$, $y \approx 0.8$. (*f*) Fully chaotic shock front, $M_0 = 2.63$, $y \approx 1.0$.

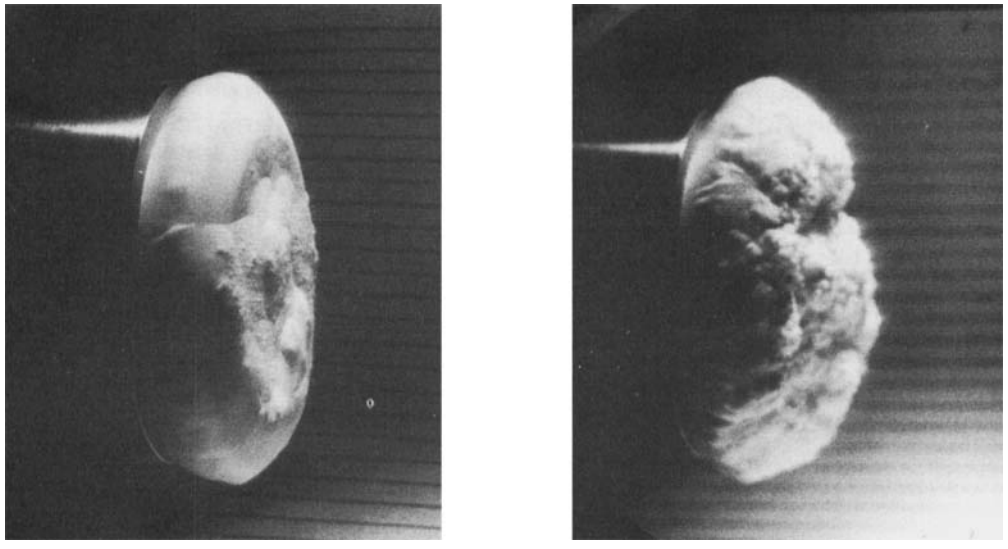

(*e*) (*f*)

FIGURE 22 (*e*, *f*). For caption see facing page.

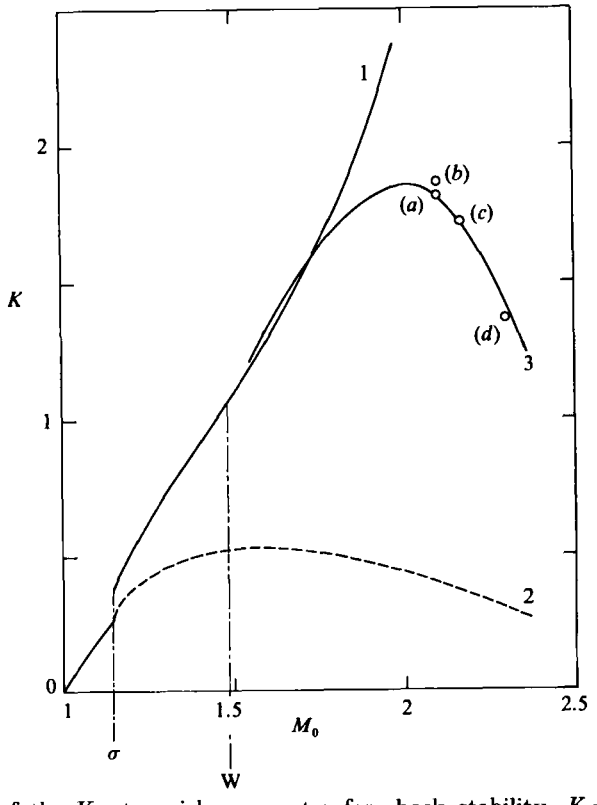

FIGURE 23. Plot of the Kontorovich parameter for shock stability, $K = (G+1)\ (v_0/v-1)\ M^2$ versus shock Mach number M_0 for FC-75 with $P_0 = 1.4$ bar, $T_0 = 120$ °C. Curve 1 is based on equilibrium two-phase sound speed, Curve 2 is based on the sound speed of the vapour phase in the mixture and 3 is based on the experimentally determined two-phase sound speed. Open circles (*a*), (*b*), (*c*), (*d*) correspond to figures 20 (*a*), (*b*), (*c*), (*d*) respectively.

9. Concluding remarks

Experiments with retrograde fluids continue to produce unanticipated and, at least for the experimenters, surprising results. We are keenly aware of the need for experiments more accurate and complete than those reported here: high-speed motion pictures of the evolving structures in an unstable shock front would be just one example.

We would like to express our gratitude for valuable assistance to Dr G. E. A. Meier, Dr Willi Moehring, Prof. F. F. Ling, Dr Jace Nunziato, Chong Yoon, Edward Boucheron, Tom DeWitt, Chris Camadella and Lisa Nasgowitz. This paper is dedicated to the memory of the late Prof. Ernst Becker of Darmstadt, who provided essential encouragement for this work. Partial support for travel was provided under National Science Foundation Grant INT-8214100.

REFERENCES

Anon 1973 Thermodynamic properties of benzene. Engineering Sciences Data Unit No. 73009, Institution of Chemical Engineers, London.

Barieau, R. E. 1966 Thermodynamic properties of a van der Waals fluid, particularly near the critical point. *Phys. Rev. Lett.* **16**, 297–300.

Barker, L. M. & Hollenbach, R. E. 1970 Shock-wave studies of PMMA, fused silica and sapphire. *J. Appl. Phys.* **41**, 4208–4226.

Batchelor, G. K. 1967 *An Introduction to Fluid Dynamics*, p. 72. Cambridge University Press.

Bethe, H. A. 1942 The theory of shock waves for an arbitrary equation of state. *Office of Scientific Research and Development, Washington, Rep. No.* 545, p. 57.

Borisov, A. A., Borisov, Al. A. & Kutateladze, S. S. 1983 Rarefaction shock wave near the critical liquid-vapour point. *J. Fluid Mech.* **126**, 59–73.

Bursik, J. W. & Hall, R. M. 1981 Generalization of low pressure, gas-liquid, metastable sound speed to high pressures. *Sixteenth Thermophysics Conference, Palo Alto, AIAA Paper* 81–1063.

Carofano, G. C. 1984 Blast computation using Harten's total variation diminishing scheme. U.S. ARDC *Tech. Rep. No.* ARLCB-TR-84029, Benet Weapons Laboratory, Watervliet, N.Y. 12189.

Chaves, H. 1980. Verdampfungswellen in retrograden Fluessigkeiten. Diplomarbeit, Georg-August-Universitaet, Goettingen.

Chaves, H. 1984 Phasenubergaenge und Wellen bei der Entspannung von Fluiden hoher spezifischer Waerme. Dissertation, Georg-August Universitaet, Goettingen.

Chen, G. 1984 Determination of the sound speed in a two-phase, vapor-liquid mixture induced by a shock wave. M.S. thesis, Rensselaer Polytechnic Institute.

Cramer, M. S. & Kluwick, A. 1984 On the propagation of waves exhibiting both positive and negative nonlinearity. *J. Fluid Mech.* **142**, 9–37.

Davidson, L. & Graham, R. A. 1979 Shock compression of solids. *Phys. Rep.* **55**, 255–379.

Dettleff, G. 1978 Experimente zum Nachweis der Verflussingungsstosswelle in retrograden Gasen. Doktorarbeit, Georg-August-Universitaet, Goettingen.

Dettleff, G., Meier, G. E. A., Speckmann, H. D., Thompson, P. A. & Yoon, C. 1982 Experiments in shock liquefaction. In *Proc. 13th Intl Symp. on Shock Tubes and Waves* (ed. C. E. Trainor & J. G. Hall), pp. 716–723. State University of New York Press.

Dettleff, G., Thompson, P. A., Meier, G. E. A. & Speckmann, H. D. 1979 An experimental study of liquefaction shock waves. *J. Fluid Mech.* **95**, 279–304.

Didden, N. 1979 On the formation of vortex rings: rolling up and production of circulation. *Z. angew. Math. Phys.* **30**, 101–116.

EHRFELD, W. 1983 *Elements of Flow and Diffusion Processes in Separation Nozzles*. Springer.

ELDER, F. K. & DE HAAS, N. 1952 Experimental study of the formation of a vortex ring at the open end of a cylindrical shock tube. *J. Appl. Phys.* **23**, 1065–1069.

FOWLES, G. R. & HOUWING, A. F. P. 1984 Instability of shock and detonation waves. *Phys. Fluids* **27**, 1982–1990.

HARTEN, A. 1983 High resolution schemes for hyperbolic conservation laws. *J. Comp. Phys.* **49**, 357–393.

HAYES, W. D. 1958 The basic theory of gasdynamic discontinuities. In *Fundamentals of Gasdynamics* (ed. H. W. Emmons), pp. 416–481. Princeton University Press.

HOBBS, D. E. 1983 A virial equation of state utilizing the principle of corresponding states. Dissertation, Rensselaer Polytechnic Institute.

JONES, D. M., MARTIN, P. M. E. & THORNHILL, C. K. 1959 A note on the pseudo-stationary flow behind a strong shock diffracted or reflected at a corner. *Proc. R. Soc. Lond.* A **209**, 238–248.

KNUTH, E. L. 1959 Nonstationary phase change involving a condensed phase and a saturated vapor. *Phys. Fluids* **2**, 84–86.

KOLSKY, H. 1969 Production of tensile shock waves in stretched natural rubber. *Nature* **224**, 1301.

KONTOROVICH, V. M. 1957 Concerning the stability of shock waves. *Sov. Phys: Tech. Phys.* **6**, 1179–1181.

KOSKY, P. G. 1968 Bubble growth measurements in uniformly superheated liquids. *Chem. Engng Sci.* **23**, 695–706.

LAMBRAKIS, K. C. 1972 Negative-Γ fluids. Dissertation, Rensselaer Polytechnic Institute.

LANDAU, L. D. & LIFSHITZ, E. M. 1959 *Fluid Mechanics*, p. 496. Pergamon.

MCQUEEN, R. G. & MARSH, S. P. 1968 Hugoniots of graphites of various initial densities and the equation of state of carbon. In *Behavior of Dense Media under High Dynamic Pressures*, pp. 207–216. Gordon and Breach.

MAXWORTHY, T. 1977 Some experimental studies of vortex rings. *J. Fluid Mech.* **81**, 465–495.

MEIER, G. E. A. & THOMPSON, P. A. 1985 Real gas dynamics of fluids with high specific heat. In *Dynamics of Real Fluids*, pp. 103–114. Springer.

MORRIS, D. G. 1980 An investigation of the shock-induced transformation of graphite to diamond. *J. Appl. Phys.* **51**, 2059–2965.

PAYMAN, W. & SHEPHERD, W. C. F. 1946 Explosion waves and shock waves, VI. *Proc. R. Soc. Lond.* A **186**, 293–321.

PLANCK, M. 1903 *Treatise on Thermodynamics*, pp. 150–152. Longmans-Green.

PUETTENDOERFER, E. 1982 Schallnaehe Stroemung eines retrograden Fluides. Diplomarbeit, Georg-August Universitaet. Goettingen.

REID, R. C., PRAUSNITZ, J. M. & SHERWOOD, T. K. 1977 *The Properties of Gases and Liquids*, pp. 199–201. McGraw-Hill.

RIZZI, A. 1982 Damped Euler-equation method to compute transonic flow around wing-body combinations. *AIAA J.* **20**, 1321–1328.

SHEPHERD, J. E. & STURTEVANT, B. 1983 Rapid evaporation at the superheat limit. *J. Fluid Mech.* **121**, 379–402.

SKEWS, B. W. 1967*a* The shape of a diffracting shock wave. *J. Fluid Mech.* **29**, 297–304.

SKEWS, B. W. 1967*b* The perturbed region behind a diffracting shock wave. *J. Fluid Mech.* **29**, 705–719.

SLEMROD, M. 1983 Admissibility criteria for propagating phase boundaries in a van der Waals fluid. *Arch. Rat. Mech. Anal.* **81**, 301–315.

SLEMROD, M. 1984 Dynamic phase transitions in a van der Waals fluid. *J. Diffl Equat.* **52**, 1–23.

SPECKMANN, H. D. 1984 Aufspaltung von Kondensationsstosswellen in Fluiden hoher spezifischer Waerme. Dissertation, Georg-August Universitaet, Goettingen.

THOMPSON, P. A. 1972 *Compressible-Fluid Dynamics*, p. 379. McGraw-Hill.

THOMPSON, P. A. 1983 Shock-wave series for real fluids. *Phys. Fluids* **26**, 3471–3474.

THOMPSON, P. A. & KIM, Y.-G. 1983 Direct observation of shock splitting in a vapor-liquid system. *Phys. Fluids* **26**, 3211–3215.

THOMPSON, P. A., KIM, Y.-G. & MEIER, G. E. A. 1984 Shock tube studies with incident liquefaction shocks. In *Proc. 14th Intl Symp. on Shock Tubes and Waves* (ed. R. D. Archer & B. E. Milton), pp. 413–420. New South Wales University Press.

THOMPSON, P. A., KIM, Y.-G. & MEIER, G. E. A. 1985 Flow visualization of a shock wave by simple refraction of a background grid. In *Optical Methods in Dynamics of Fluids and Solids*, pp. 225–231. Springer.

THOMPSON, P. A. & LAMBRAKIS, K. C. 1973 Negative shock waves. *J. Fluid Mech.* **60**, 187–208.

THOMPSON, P. A. & SULLIVAN, D. A. 1975 On the possibility of complete condensation shock waves in retrograde fluids. *J. Fluid Mech.* **70**, 639–650.

TSONOPOULOS, C. 1974 An empirical correlation of second virial coefficients. *Am Inst. Chem. Engng J.* **20**, 263–272.

VAN DER WAALS, J. D. 1908 *Lehrbuch der Thermodynamik*. Bearbeitet von Ph. Kohnstamm, Maas und Van Suchtelen, Leipzig.

VAN DYKE, M. 1982 *An Album of Fluid Motion*, pp. 148, 242. Parabolic.

WEGENER, P. P. & MACK, L. M. 1958 Condensation in supersonic and hypersonic wind tunnels. In *Advances in Applied Mechanics*, vol. 5 (ed. H. L. Dryden & Th. von Kármán), pp. 307–447. Academic.

WEGENER, P. P. & WU, B. J. C. 1977 Gasdynamics and homogeneous nucleation. *Adv. Colloid Interface Sci.* **7**, 325–417.

YAMADA, T. 1973 An improved generalized equation of state. *AIChE.J.* **19**, 286–291.

YARRINGTON, R. M. & KAY, W. B. 1960 Thermodynamic properties of perfluoro-2-butyltetrahydrofuran. *J. Chem. Engng Data* **5**, 24–29.

YEE, H. C., WARMING, R. F. & HARTEN, A. 1982 A high resolution numerical technique for inviscid gas-dynamic problems with weak shocks. In *Proc. 8th Intl Conf. Numerical Methods in Fluid Dynamics, Aachen, West Germany*. Springer.

YEE, H. C., WARMING, R. F. & HARTEN, A. 1983 Implicit total variation diminishing (TVD) schemes for steady-state calculations. *NASA Tech. Mem.* 84342.

YOON, C. 1985 Shock liquefaction experiments with retrograde substances. Dissertation, Rennselaer Polytechnic Institute.

ZEL'DOVICH, YA. B. 1946 On the possibility of rarefaction shock waves. *Zh. Eksp. Teor. Fiz.* **4**, 363–364.

ZEL'DOVICH, YA. B. & RAIZER, YU. P. 1967 *Physics of Shock Waves and High-Temperature Hydrodynamic Phenomena*. Vol. 2 (ed. W. D. Hayes & R. F. Probstein), pp. 750–756. Academic.